JGR Atmospheres

RESEARCH ARTICLE
10.1029/2021JD035845

Key Point:

- A joint analysis between ground radar, space-borne radar, and disdrometers to quantify precipitation processes in a tropical cyclone

Correspondence to:
N. S. Brauer,
nbrauer@ou.edu

Citation:
Brauer, N. S., Alford, A. A., Waugh, S. M., Biggerstaff, M. I., Carrie, G. D., Kirstetter, P. E., et al. (2022). Hurricane Laura (2020): A comparison of drop size distribution moments using ground and radar remote sensing retrieval methods. *Journal of Geophysical Research: Atmospheres*, *127*, e2021JD035845. https://doi.org/10.1029/2021JD035845

Received 20 SEP 2021
Accepted 14 JUL 2022

Hurricane Laura (2020): A Comparison of Drop Size Distribution Moments Using Ground and Radar Remote Sensing Retrieval Methods

Noah S. Brauer[1,2], A. Addison Alford[3,4], Sean M. Waugh[4], Michael I. Biggerstaff[1,2,3], Gordon D. Carrie[1], Pierre E. Kirstetter[1,2,4], Jeffrey B. Basara[1,5], Daniel T. Dawson[6], Kimberly L. Elmore[3,4], Jeffrey Stevenson[1], and Robert W. Moore[1]

[1]School of Meteorology, The University of Oklahoma, Norman, OK, USA, [2]Advanced Radar Research Center, Norman, OK, USA, [3]Cooperative Institute for Severe and High-Impact Weather Research and Operations, The University of Oklahoma, Norman, OK, USA, [4]NOAA National Severe Storms Laboratory, Norman, OK, USA, [5]School of Civil Engineering and Environmental Science, The University of Oklahoma, Norman, OK, USA, [6]Department of Earth, Atmospheric and Planetary Sciences, Purdue University, Norman, OK, USA

Abstract Hurricane Laura was the strongest hurricane to make landfall in Louisiana since 1969 with maximum sustained winds of 130 knots. One University of Oklahoma Shared Atmospheric Mobile and Teaching Polarmetric Radar (SR1-P), and four portable in situ precipitation stations (PIPSs) equipped with parsivel disdrometers were spatially and temporally collocated with two NASA Global Precipitation Measurement Mission Dual-frequency Precipitation Radar overpasses. The combined retrieval methods were able to quantify and compare drop size distribution moments and radar-inferred precipitation processes before, during, and after the storm center made landfall. It was found that the magnitude of collision-coalescence dominant precipitation decreased from before to after landfall. Further, the presence of a bright-band becomes more evident across all percentiles in the post-landfall overpass, indicating an increase in stratiform precipitation compared to convective precipitation after Laura moved inland. The PIPS showed an increase in mean drop size from 1.0 mm before landfall to as high as 4.0 mm in the eyewall, while decreasing to below 1.0 mm as Laura continued to move inland with a decrease in maximum echo top height of 0.5–1.0 km. Last, the Dual-frequency Precipitation Radar (DPR) algorithm overestimated the normalized intercept parameter by 0.5–1.0 m^{-3} mm^{-1} compared to the PIPS implying differences in measured drop number concentration, potentially due to differences in measurement footprint or assumptions in the DPR retrieval algorithm. These findings can potentially be used to improve the DPR particle size distribution algorithm in tropical cyclones.

Plain Language Summary Understanding the dominant precipitation processes in tropical cyclones (TCs) is important for quantifying the potential for flash flooding in warning operations and improving precipitation forecasts from numerical models. Hurricane Laura (2020) provided a unique opportunity to analyze precipitation processes throughout its evolution as numerous radars and instruments were deployed in various portions of the storm. As each observational method has advantages and disadvantages, a joint analysis between all sensors allows for a direct comparison of rainfall characteristics to better understand the evolution and distribution of precipitation in landfalling TCs. The results suggest that the space-borne radar may be overestimating rainfall concentration compared to the ground-based instruments, and considerable variations in raindrop size occurred between the outer portions of the storm compared to the storm center.

1. Introduction

Landfalling tropical cyclones (TCs) are known to produce catastrophic damage from wind, heavy rainfall, and storm surge (e.g., Rappaport, 2000, 2014). While wind damage is typically the main focus of TCs, Rappaport (2014) found that water-related deaths accounted for 90% of landfalling Atlantic TC fatalities. Therefore, it is important to understand and quantify processes associated with excessive precipitation in TCs.

Microphysics in TCs are uncertain and observations often disagree with numerical simulations, which poses a challenge toward understanding TC structure, evolution, and intensity (e.g., Chen & Gopalakrishnan, 2014; Hristova-Veleva et al., 2021). Prior observational studies have shown that collision-coalescence and drop breakup are the dominant precipitation processes in warm rain events such as TCs (e.g., Atlas & Ulbrich, 2000; List

et al., 1987). Polarimetric radar observations are useful in cases of landfalling TCs due to their high temporal resolution and large sampling domain (e.g., Didlake Jr. & Kumjian, 2018; Medlin et al., 2007), and can provide useful insight into dominant precipitation processes. This can be particularly beneficial in forecasting/nowcasting operations (e.g., Cunha et al., 2013; Giangrande et al., 2008; Straka et al., 2000) and can be used for more accurate rainfall rate estimations compared to conventional Z-R relationships (Ryzhkov, Giangrande, & Schuur, 2005; You et al., 2019). Didlake and Kumjian (2017) analyzed polarimetric radar signatures to infer precipitation microphysical processes in Hurricane Arthur (2014), and determined that the highest values of low-level differential reflectivity (Z_{DR}) occurred in the outer rainbands, whereas the lowest Z_{DR} occurred in the inner rainbands and eyewall. This implies significant changes in the drop size distribution as a function of distance from the hurricane center. It has also been shown that there is typically a maximum in specific differential phase (K_{DP}) displaced downwind from the relative maximum in Z_{DR} that occurs in the eyewall which is indicative of hydrometeor size-sorting (e.g., Feng & Bell, 2019; Homeyer et al., 2021; Laurencin et al., 2020). This process occurs as smaller drops have a lower terminal velocity and are therefore advected further downwind, whereas larger hydrometeors fall out of the cloud at a faster rate (Kumjian & Ryzhkov, 2012). DeHart and Bell (2020) found that polarimetric radar observations in Hurricane Harvey (2017) and Hurricane Florence (2018) exhibited signatures associated with large concentrations of small and medium drops, with Harvey having the greatest particle size distribution (PSD) variability over time. These are similar to the results from Zheng et al. (2021), who also concluded that collision-coalescence and accretion are the dominant processes in mature inner rainbands. Further, Tokay et al. (2008) analyzed landfalling TCs from three disdrometer sites from 2004 to 2006 and found that all TCs contained large concentrations of small to medium-sized drops except when each storm had undergone extratropical transition. This is also consistent with Homeyer et al. (2021), who showed a variation in mass-weighted mean drop diameter (D_M) ranging from 0.5 to 2.0 mm at various points in time throughout the evolution of Hurricane Harvey (2017) and Hurricane Florence (2018). Last, Brauer et al. (2020) found that training supercell thunderstorms in the outer rainbands of Hurricane Harvey contained large concentrations of medium-sized drops which contributed to the excessive precipitation event over the region.

Spatially within TCs, McFarquhar and Black (2004) analyzed two events and determined that there is a large variation in the drop size distribution from stratiform to convective regions. Prior work from Cecil et al. (2002) showed that Z_H increases toward the surface within the warm cloud layer, particularly in the inner core of TCs. Kumjian and Ryzhkov (2012) and Carr et al. (2017) attributed this decrease in Z_H with height with collision-coalescence or a balance between collision-coalescence and drop breakup depending on the slope of Z_{DR} within the same layer. While dominant precipitation processes can be inferred from ground-based polarimetric radar observations, coarse vertical resolution and beam-broadening at a large range limits the extent in which these signatures can be captured. For this reason, it is useful to complement ground-radar observations with space-borne radar retrievals which have a much finer vertical resolution and can provide vertical profiles of reflectivity and extracted PSD moments at snapshots in time (e.g., Hou et al., 2014; Porcacchia et al., 2019; Skofronick-Jackson et al., 2017). Additionally, space-borne radars such as the NASA global precipitation measurement (GPM) mission dual-frequency precipitation radar (DPR) tend to be much better calibrated compared to ground radars (Warren et al., 2018).

The tropical rainfall measurement mission (TRMM) was the first space-borne radar to sample precipitation in TCs after becoming operational in 1997 (Kummerow et al., 1998), and was able to properly identify the spatial and temporal variations in TCs in the low latitudes (Jiang et al., 2011). Since TRMM, the NASA GPM mission DPR was launched in February 2014 and is equipped with both Ku and Ka-band active sensors, and is capable of sampling TCs at higher latitudes, whereas TRMM was confined to 35°N/S (Hou et al., 2014; Skofronick-Jackson et al., 2017). Huang and Chen (2019) analyzed 68 TCs in the Western North Pacific using the DPR and determined that the 2 km D_M was larger in regions of convection compared to areas of stratiform precipitation. It was also found that in regions of high precipitation efficiency, Ku-band reflectivity (KuPR) and D_M increased toward the surface below the melting layer in both convective and stratiform areas implying drop growth via collision-coalescence. A similar framework was used by Porcacchia et al. (2019) who investigated the slopes of KuPR and KaPR from the DPR and Z_H and Z_{DR} from ground radars in warm rain events and found that precipitation events that were characterized primarily by collision-coalescence typically have a lower ice content above the 0 C than non-collision-coalescence cases.

Numerical simulations of Hurricane Rita (2005) were compared to TRMM space-borne radar retrievals, and showed that model output overestimated the magnitude of ice content compared to the observations (Hristova-Veleva et al., 2021). They further showed that the assumed PSD algorithm intercept parameter (N_0) used in the weather research and forecasting model simulations resulted in differences between the observed and modeled reflectivity. Due to the known differences between PSD estimates from the space-borne radar retrievals in TCs and ground-based radar observations, in situ disdrometers can be used to calibrate polarimetric radar observations to precipitation moments in order better refine the DPR PSD algorithm (e.g., Liao et al., 2014; Radhakrishna et al., 2016).

Ground-based disdrometer retrievals and aircraft-mounted optical array probe observations have historically been used to empirically derive Z_H-weighted rainfall rate relationships in TCs, commonly known as Z-R relationships (e.g., Jorgensen & Willis, 1982; Ulbrich & Lee, 2002; Wilson & Pollock, 1974). However, microphysical and precipitation processes near the surface using ground radars can only be inferred as these retrievals are prone to discrete sampling due to beam broadening, attenuation at higher frequencies such as C-band and X-band, partial beam filling, and increasing beam height with range (e.g., Kirstetter et al., 2013; Ryzhkov, 2007; Zhang et al., 2013). Therefore, it is important to obtain observations at the ground to more accurately quantify PSD moments. Many field campaigns have compared mobile radar retrievals to disdrometer observations and have found differences between radar reflectivity and disdrometer-derived reflectivity for these reasons (e.g., Kalina et al., 2014; Sheppard & Joe, 1994). Merceret (1974) gathered aircraft foil impactor measurements in Hurricane Ginger (1971), and found that an exponential distribution provided an accurate fit for the PSD, which is also true in other cases as uncertainties are higher when using a gamma distribution to estimate PSD moments (Smith, 2003). A network of 2D video disdrometers, a Joss–Waldvogel disdrometer, and OTT parsivel disdrometers in Huntsville, AL sampled precipitation events over 6 months and found that when $D_M < 0.76$ mm, the Parsivel disdrometers greatly underestimated drop concentration (Tokay et al., 2013). Further, the same study concluded that PSDs that were skewed by drops >2.4 mm yields an overestimation of drop concentration. Another study compared OTT parsivel disdrometers with 2D video disdrometers for 36 rainfall events in South Korea, where the Parsivels were found to overestimate D_M when using a gamma distribution while underestimating the magnitude of $\log_{10}(N_w)$ (Park et al., 2017). With the known disadvantages of the parsivel disdrometers such as a high uncertainty of PSD quantities at a $D_M > 5$ mm in addition to a high bias in $\log_{10}(N_w)$ at values of $D_M > 2.4$ mm, these in situ observations can be used to calibrate both ground and space-borne radar retrievals of PSD moments (e.g., Lee & Zawadzki, 2006; Tokay et al., 2013). GPM DPR retrievals were compared to disdrometer observations in China, and it was shown that stratiform precipitation regions in warm season rainfall events showed the largest values of N_0, slope parameter (Λ), and shape factor (μ) compared to areas of convection and winter precipitation cases (Wu et al., 2019). Disdrometer observations from seven Atlantic TCs were collected from 2004 to 2006 and showed that D_M was largely lower than 4 mm and PSDs consisted of a large concentration of small drops throughout the entire TC evolution before extratropical transition (Tokay et al., 2008). As disdrometer observations frequently suffer from measurement and sampling biases, it is useful to compare the portable in situ precipitation station (PIPS) retrievals to ground and space-borne radar observations to more accurately quantify the evolution and magnitude of PSD moments throughout different portions of Hurricane Laura before, during, and after landfall. While the comparison between remote sensing retrievals and disdrometer observations is useful, the differences in horizontal footprints between the GPM DPR (5 km), SR1-P (37.5 m gates), and point observations from the PIPS must be considered.

Given the importance of accurately predicting the water threat that TCs pose, combined with the uncertainties of radar observations (particularly at the low levels), and the general lack of detailed in situ observations near the surface, a need exists for an in depth look at available remote data sources compared to direct observations. Such a detailed look would provide valuable insight into the Z-R relations used in TC forecasting/nowcasting and allow for a more accurate threat representation when viewing remote sensing observations (such as radar) during events. Further, an improved understanding of TC microphysics would benefit future microphysical parameterization schemes in numerical models to better predict TC structure and evolution.

The combination of one OU-CIMMS polarimetric C-band Shared Mobile Atmospheric Research and Teaching (SMART) polarimetric radar (SR1-P) (Biggerstaff et al., 2005), four PIPSs (Dawson et al., 2017) equipped with parsivel laser disdrometers (locations shown in Table 1), and two overpasses from the GPM DPR provides a novel framework for quantifying various drop size distribution characteristics and precipitation microphysics

Table 1
Table With Portable In Situ Precipitation Stations (PIPS) Locations and Starting Time

PIPS number	Latitude	Longitude	Starting time
PIPS1A	30.224910	−93.518746	1942 UTC
PIPS1B	30.26642	−93.359979	2019 UTC
PIPS2A	30.245168	−92.928744	2206 UTC
PIPS2B	30.246739	−92.739726	2148 UTC

in a landfalling TC. Each retrieval method provides unique advantages such as a high temporal resolution from the ground radar observations and disdrometers in addition to a fine vertical sampling from the GPM DPR. Thus, the disadvantages of each observation platform can be complemented by the aforementioned advantages of all retrieval methods. This study aims to quantify the hypothesized difference in PSD moments that are extracted by the DPR algorithm with the disdrometer observations that were collected before, during, and after the landfall of Hurricane Laura.

2. Data and Methods

2.1. Event Background

Hurricane Laura developed from an African easterly wave that entered the northeastern Caribbean Ocean on 22 August 2020, and interacted with the higher terrain of Hispaniola and Puerto Rico as a tropical storm before entering the Gulf of Mexico. As Laura moved off Cuba into the Gulf of Mexico on 25 August, the storm began rapid intensification and reached a peak intensity as a Category 4 hurricane with maximum sustained winds of 130 knots and a minimum central pressure of 937 hPa on 27 August (National Hurricane Center, 2021). Laura made landfall near Cameron, Louisiana at 0600 UTC 27 August as a Category 4 major hurricane and caused severe wind damage to the Lake Charles, LA and surrounding area, including the Lake Charles radar (KLCH). Freshwater flooding and storm surge flooding occurred close to the landfall point in Calcasieu Parish, LA where 12" of rain fell. Additional flooding occurred further inland over southern Arkansas as Laura tracked north (National Hurricane Center, 2021).

2.2. Ground-Based Radar Observations

The KLCH WSR-88D (30.13°N, −93.22°W) operates at S-band (10 cm) and was used in conjunction with a SMART C-band radar (SR1-P, 5 cm) located at 30.36°N, −92.92°W in the anticipated landfall zone. SR1-P collected polarimetric radar observations of Z_H, Z_{DR}, K_{DP}, and ρ_{hv} from 1942 UTC 26 August to 1200 UTC 27 August. Due to wind gusts in excess of 120 mph, the KLCH radar stopped operating at 0553 UTC 27 August as the inner core of Laura moved onshore and the radar sustained catastrophic damage.

The radar reflectivity factor at a horizontal polarization (Z_H) provides insight into the size and concentration of hydrometeors within a range bin (e.g., Austin, 1987; Herzegh & Jameson, 1992; Kumjian, 2013a; Vitale & Ryan, 2013; Zrnic & Ryzhkov, 1999). Differential reflectivity (Z_{DR}) is defined as the logarithmic ratio of the horizontal reflectivity factor to the vertical reflectivity factor, and provides information regarding the size, shape, and orientation of hydrometeors (e.g., Herzegh & Jameson, 1992; Kumjian, 2013a; Seliga & Bringi, 1976). Specific differential phase (K_{DP}) is defined as one half the range derivative of the propagation differential phase shift, and reveals information about the number concentration of hydrometeors in a sample volume (e.g., Herzegh & Jameson, 1992; Kumjian, 2013b; Ryzhkov, Giangrande, & Schuur, 2005; Zrnic & Ryzhkov, 1999) and is immune to attenuation and radar miscalibration assuming uniformly distributed scatterers (e.g., Jameson, 1985; Seliga & Bringi, 1978; Wang & Chandrasekar, 2009) making it a useful variable for quantitative precipitation estimation. Lastly, ρ_{hv} can be used to quantify the diversity of scatterers, to distinguish meteorological versus non-meteorological returns (e.g., Herzegh & Jameson, 1992; Kumjian, 2013a; Ryzhkov, Giangrande, & Schuur, 2005; Ryzhkov, Schuur, et al., 2005; Zrnic & Ryzhkov, 1999), and identify features such as the melting layer (e.g., Kumjian, 2013a; Kumjian, 2013b). A uniform PSD will yield a ρ_{hv} near 1, whereas mixed-phase precipitation results in $\rho_{hv} < 0.95$ (e.g., Herzegh & Jameson, 1992; Kumjian, 2013a; Ryzhkov, Giangrande, & Schuur, 2005; Ryzhkov, Schuur, et al., 2005; Zrnic & Ryzhkov, 1999).

Range height indicator (RHI) scans from SR1-P were collected over the PIPS and plotted from 0211 to 0259 UTC 27 August at an azimuth angle of 160°, and from 0510 to 0541 UTC at an azimuth angle of 220°. Time-averaged mean RHIs of Z_H, Z_{DR}, and ρ_{hv} were computed over both time periods and azimuth angles in order to gain insight into the dominant precipitation processes at different stages in the evolution of Laura shortly before landfall. Further, RHIs provide a high vertical resolution and insight into the connection between precipitation features aloft and near the surface. In order to account for Z_{DR} miscalibration, a bias correction method documented in Sanchez-Rivas and Rico-Ramirez (2021) was employed. "Bird bath" style Z_{DR} calibration requires data to be

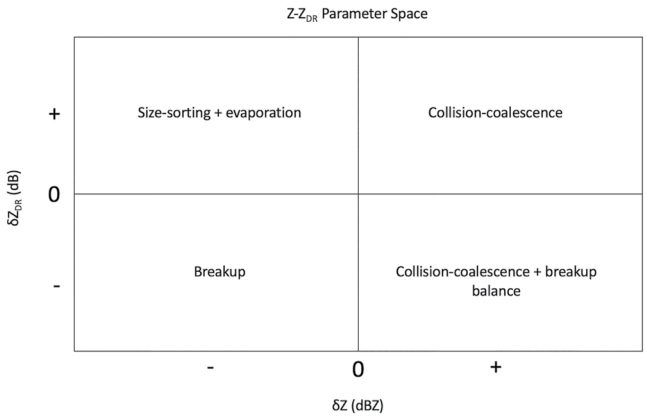

Figure 1. Z-Zdr Parameter Space developed by Kumjian and Ryzhkov (2012) that uses changes in Z_H and Z_{DR} within the warm cloud layer to identify dominant precipitation processes.

collected at 90° elevation (Gorgucci et al., 1992), but such data were not collected during the SR1-P observation period in Hurricane Laura. Likewise, the Z_{DR} calibration method of Ryzhkov, Giangrande, Melnikov, and Schuur (2005) is not applicable, as it requires PPIs between 40 and 60° elevation to be utilized. Again, no such data were collected. Thus, the method of Sanchez-Rivas and Rico-Ramirez (2021) is optimal, as their method utilizes quasi-vertical profiles (QVPs) (Ryzhkov et al., 2016) collected in light rain to estimate the Z_{DR} bias. The Sanchez-Rivas and Rico-Ramirez (2021) method utilizes a QVP constructed at the 10° elevation angle and uses data where Z_H is between 0 and 20 dBZ and where $\rho_{hv} > 0.985$. While their method employs the use of data between the first radar range gate and the melting level (characterized by an objective algorithm), we take a simpler approach and only employ QVP data between 1 and 4 km altitude, below the radar bright band. While there was only one QVP where such criteria were met, a bias of −1.7 dB was computed for this case, which is a typical bias for SR1-P (e.g., Biggerstaff et al., 2021). As drops in hurricanes are typically small (as evidenced in this manuscript) and to include a greater number of QVPs to test the sensitivity of the computed bias to the number of observations, we also extended the method to include data characterized by 0–25 dBZ (0–30 dBZ) and found a similar Z_{DR} bias of −1.7 dB (−1.8 dB). To remain consistent with Sanchez-Rivas and Rico-Ramirez (2021), we add −1.7 dB to all Z_{DR} observations herein. The large calibration bias is due to a bad input parameter that was embedded in the proprietary software during the dual-polarization upgrade. Rather than attempt to find and replace the parameter, we chose to perform the calibration in post-processing.

Additionally, plan position indicator (PPI) scans of Z_H from SR1-P were plotted at 0230 UTC and 0525 UTC on 27 August with the locations of the associated RHI scans. Finally, columnar-vertical profiles (CVPs) of Z_H, Z_{DR}, K_{DP}, and ρ_{hv} from SR1-P were plotted from 0200 to 1000 UTC 27 August which used the methodology from Murphy et al. (2020). The CVPs were constructed using a Cressman weighting function (Cressman, 1959) to transform from an irregular height grid to a regular (50 m) height grid. Further, the CVPs were conducted directly over PIPS 2A and were based on a 10 km (10°) range (azimuth), with a Cressman radius limit of 100 m. One potential limitation of the CVP method is that the Cressman weighting function that was used can still resulting in vertical gaps in polarimetric radar data.

Dominant precipitation processes were determined by examining the sign of slopes of vertical profiles of Z_H and Z_{DR} within the warm cloud layer based off the framework from Kumjian and Ryzhkov (2012) (Figure 1). For example, collision-coalescence dominant precipitation would be identified in vertical profiles where both Z_H and Z_{DR} increase toward the surface below the melting layer, implying the presence of drop growth.

2.3. GPM Dual-Frequency Precipitation Radar

The NASA GPM mission was launched in 2014 and operated similarly to the TRMM, which ended in 2015 (Hou et al., 2014; Skofronick-Jackson et al., 2017). On board the GPM platform is the DPR, which operates at Ku and Ka-bands (35.5 and 13.6 GHz) (Hou et al., 2014; Skofronick-Jackson et al., 2017) and can provide snapshots of the precipitation structure in TCs on a global scale (e.g., Huang & Chen, 2019; Marra et al., 2019; Brauer et al., 2021). The radar has a swath width of 245 km, a vertical resolution of 250 m, and a horizontal resolution of 5.2 km (Hou et al., 2014; Skofronick-Jackson et al., 2017). The DPR algorithm extracts PSD moments such as the mass-weighted mean drop diameter (D_M) (mm) and the normalized intercept parameter ($\log_{10}(N_w)$) (m^{-3} mm^{-1}) which relates to hydrometeor concentration, and assumes a gamma distribution in liquid phase precipitation (Equation 1), where N_0 (m^{-3} mm^{-1}) is the intercept parameter and D_0 (mm) is the median volume diameter. D_M can then be related to D_0 using Equation 2, which can be used to compute $\log_{10}(N_w)$. More information regarding the DPR algorithm to estimate PSD moments can be found here: (https://gpm.nasa.gov/sites/default/files/document_files/ATBD_GPM_DPR_n3_dec15.pdf). Further, the GPM DPR surface reference for attenuation correction that is used over land is less reliable than over the open ocean, resulting in some uncertainties in near-surface PSD retrievals (Meneghini et al., 2015). However, recent advances in the DPR PSD algorithm (version 4) suggests that KuPR has a probability of detection of 0.967 in surface rainfall rates greater

than 1 mm h^{-1} over flat terrain (Speirs et al., 2017). Additionally, Liao and Meneghini (2019) determined that D_M biases from the DPR are generally <0.5 mm across the entire PSD. Cannon et al. (2017) also showed the utility of the DPR in estimating precipitation over the ocean in the eastern North Pacific Ocean, with accurate representations of the bright-band height when compared to reanalysis data and ground radars.

$$N(D) = N_0 D^{\mu} \exp\left[-\frac{(3.67+\mu)D}{D_0}\right] \tag{1}$$

$$D_0 = \left(\frac{3.67+\mu}{4+\mu}\right) D_M \tag{2}$$

Along-track cross-sections of KuPR, D_M, and $\log_{10}(N_w)$ were plotted from the available DPR overpasses that occurred from 0228 to 0401 UTC and 1144 to 1316 UTC 27 August (Figures 6 and 7). Additionally, attenuation-corrected near-surface KuPR is shown to illustrate the cross-section locations and the spatial distribution of precipitation after Laura made landfall. The DPR-extracted 0 C isotherm was also included on each cross-section to quantify the height of the melting level and to provide a direct comparison with the ground radar retrievals. Additionally, vertical profiles of 25th, 50th, 75th, and 95th quantiles of KuPR were computed to illustrate the slope of reflectivity below the melting level to infer collision-coalescence and/or drop breakup processes (Porcacchia et al., 2019).

2.4. Portable In Situ Precipitation Stations (PIPS)

Four PIPS were deployed to Hurricane Laura which measured temperature, dewpoint temperature, wind speed at 1.2 m AGL, pressure, drop terminal velocity, drop size, and drop concentration, and were strategically placed in different locations relative to the landfall point in order to sample PSDs in different portions of the storm. Efforts were made to ensure that each PIPS was located away from ground clutter such as trees, power lines, and buildings that may contaminate the PSD retrievals. Each PIPS collected data for approximately 17 hr, spanning the before, during, and post-landfall periods of Laura. PIPS1B recorded a minimum pressure of 949.8 mb which experienced the eye and northwestern eyewall. While PIPS1A was close in proximity to PIPS1B, it was far enough west to only experience the western portion of the eyewall. Only PIPS2A sampled the eastern eyewall with PIPS2B sampling the outer edge of the inner core and outer rainbands, with PIPS1A, PIPS1B, and PIPS2A all experiencing peak winds greater than 30 ms^{-1} as Laura made landfall. Time series of drop diameter and total drop concentration $\log_{10}(N_T)$ were plotted from PIPS1A (0000–0650 UTC 27 August), 2A (0000–1200 UTC 27 August), and 2B (0000–1200 UTC 27 August) as PIPS1B experienced a data corruption issue during landfall. It is important to make the distinction between $\log_{10}(N_W)$ and $\log_{10}(N_T)$, which is expressed mathematically below (Equation 3) where N_0 (m^{-3} mm^{-1}) is the normalized intercept parameter, Γ is the Gamma function, μ is the shape factor, and Λ is the slope parameter (unitless). Further, the D_M was plotted for the aforementioned PIPS for each time period in order to provide a direct comparison with the D_M that was extracted by the DPR. Time series of D_M were plotted using a Gamma distribution as described in Tokay and Short (1996). $\log_{10}(N_W)$ was also computed (Equation 4) to provide a direct comparison with the DPR retrievals, where ρ_w is the density of water (g cm^{-3}) and W is the liquid water content (g m^{-3}). For clarification, the PIPS measured $\log_{10}(N_T)$ directly, whereas $\log_{10}(N_W)$ was computed to provide the comparison with the DPR algorithm derived $\log_{10}(N_W)$. Additionally, Z_H and Z_{DR} were computed from the T-matrix method (Vivekanandan et al., 1991) using a C-band wavelength of 5.34 cm to directly compare the SR1-P radar observations to the disdrometer estimations. These values were then compared to 0.8° scans from SR1-P where linear spatial means of the nearest 50 range gates of Z_H and Z_{DR} closest to the PIPS were computed and plotted as time series. A 50 range gate average was computed as the Z_H and Z_{DR} field was relatively uniform in close proximity at points in time and data quality decreases with increasing range. As the SR1-P data have a gate spacing of 75 m, the distance from the ground radar to PIPS 1A was 60 km, 12 km to PIPS 2A, and 21 km to PIPS 2B.

$$N_T = N_0 \frac{\Gamma(\mu+1)}{\Lambda^{\mu+1}} \tag{3}$$

$$log_{10}(N_W) = log_{10}\left(\frac{4^4 1000^3}{\pi \rho_w}\left(\frac{W}{(D_M)^4}\right)\right) \tag{4}$$

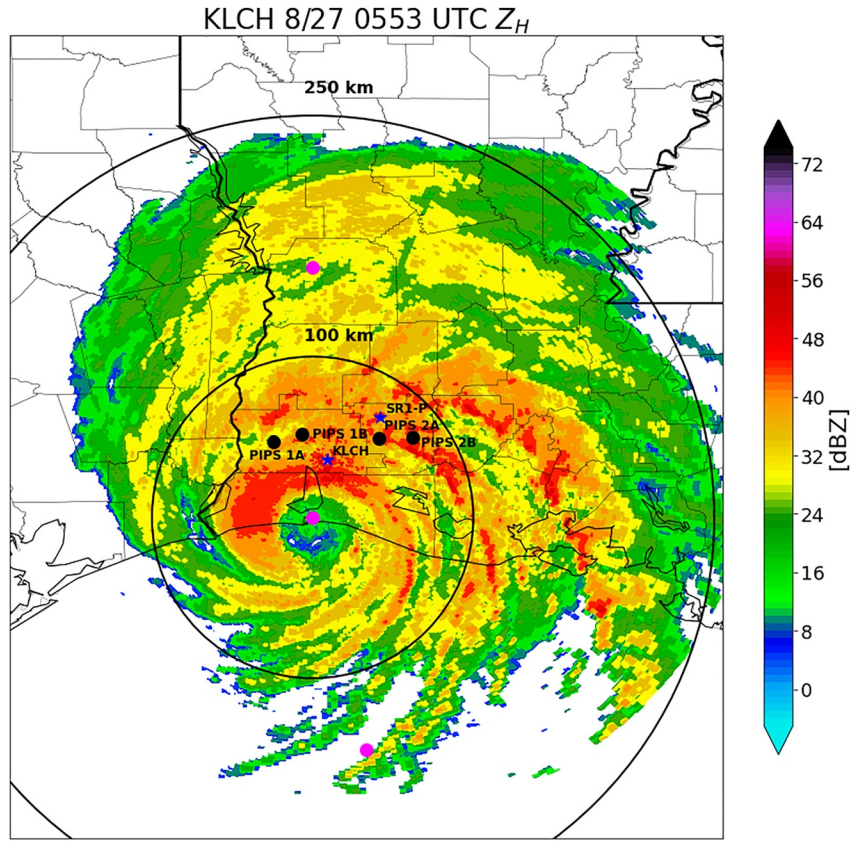

Figure 2. Raw image of 0.5° Z_H at 0553 UTC 27 August, shortly before the Lake Charles radar (KLCH) WSR-88D went down. Overlaid are the locations of the four portable in situ precipitation station, SR1-P, and the KLCH WSR-88D. Additionally, HURDAT2 best track points are shown in magenta to illustrate the track of Laura (Science Applications International Corporation and National Hurricane Center (1993)). The 100 and 250 km range rings are centered on the storm center at the time of the plan position indicator.

The parsivel disdrometer data were quality controlled to remove drops affected by splashing of drops off the instrument, and records that contain drops shed from the surrounding instruments on the PIPS following similar methodology to Friedrich et al. (2013). Drops that were 50% of the Atlas et al. (1973) drop fall speed relation were also removed to assure that all drops passing through the disdrometer were falling as rain drops, rather than drops rolling over the edge of the parsivel. Further quality control was applied by limiting parsivel records based on the wind direction through the parsivel opening. Only times when the on board sonic anemometer registered the wind direction being within 45° from the line normal to the plane laser were retained.

3. Results

3.1. Ground Radar Observations

Figure 2 shows a PPI of 0.5° Z_H from the KLCH radar at 0553 UTC, as Laura made landfall on the southwestern Louisiana coast shortly before the WSR-88D become non-operational due to strong winds. At this time the PIPS were able to sample the inner core of Laura, defined as the region between 0 and 100 km from the TC center (Weatherford & Gray, 1988), with corresponding values of Z_H from the WSR-88D ranging from 40 to 50 dBZ. Before landfall at 0230 UTC 27 August, SR1-P began sampling the outer core with Z_H values in a similar range of 40–50 dBZ (Figure 3a). Shortly before landfall at 0525 UTC 27 August, SR1-P was located in the inner core of Laura experiencing Z_H as high as 55 dBZ and sampled the northern half of the eyewall (Figure 3b). The corresponding black lines represent the orientation of the RHIs that were taken as Laura progressed northward across southwestern Louisiana. Time-averaged RHI scans of Z_H (Figure 4a), Z_{DR} (Figure 4b), and ρ_{hv} (Figure 4c) from SR1-P from 0211 to 0259 UTC 27 August and 0510–0541 UTC 27 August (Figures 4d–4f) were also plotted to

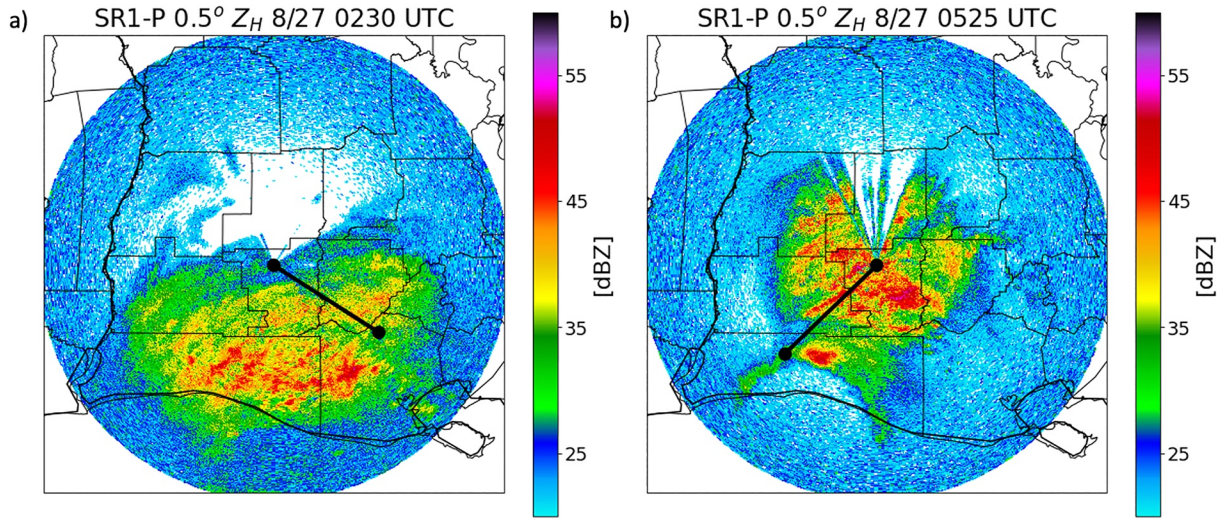

Figure 3. (a) PPIs of Z_H from SR1-P at 0230 UTC and (b) 0525 UTC on 27 August during the times of both range height indicator (RHI) composites in Figure 4. The black lines denote the locations of each RHI cross-section of 70 km.

gain insight into how the polarimetric radar variables changed with height. Between 0211 and 0259 UTC, SR1-P captured an increase in Z_H from 45 to 50 dBZ toward the surface at a beam height of 2–3 km and distance of 50–60 km from the radar (Figure 4a). This location from the radar also exhibited a decrease in Z_{DR} toward the surface within the same layer implying a balance between collision-coalescence and drop breakup (e.g., Carr et al., 2017; Kumjian & Ryzhkov, 2012; Porcacchia et al., 2019) (Figure 4b). During this time window, the

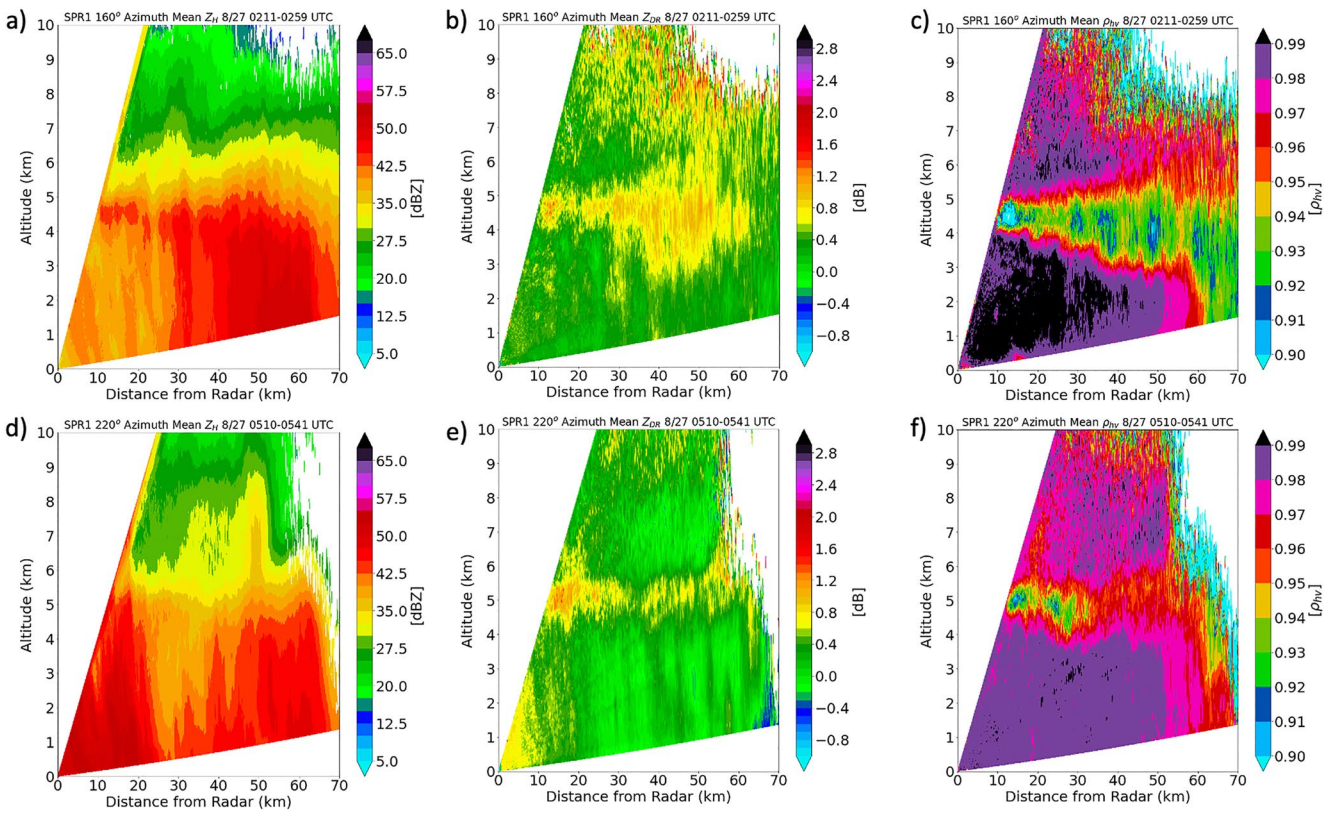

Figure 4. (a) Time averaged mean Z_H, Z_{DR}, and ρ_{hv} from SR1-P at an azimuth angle of 160° from 0211 to 0259 UTC on 27 August and (b) at an azimuth angle of 220° at 0510–0541 UTC on 27 August. Precipitation processes are inferred from the change in Z_H and Z_{DR} toward the surface below the melting layer.

melting layer was located at a height of 4.5 km as noted by the region of $\rho_{hv} < 0.98$ (Figure 4c). While the layer of $\rho_{hv} < 0.98$ continued to decrease in elevation beyond 25 km, this is likely an artifact of radar beam broadening rather than a decrease in melting layer height with range.

Shortly before landfall from 0510 to 0541 UTC 27 August, SR1-P exhibited an increase in Z_H toward the surface below the melting layer throughout the entire depth of the warm cloud layer (Figure 4d). Subtle increases in Z_{DR} from 0.0 to 0.5 dB toward the surface were also observed, particularly at a distance of 40–60 km from the radar (Figure 4e). The combination of both Z_H and Z_{DR} increasing toward the surface within the warm cloud layer implies the dominance of collision-coalescence processes during this time. Additionally, the height of the melting layer also increased to 4.5–5.0 km throughout this time period, which is 0.5 km higher in altitude compared to 3 hr prior (Figure 4f). This is likely due to latent heat release in convection in the eyewall as it moved within range of SR1-P (Kirstetter et al., 2013).

Columnar-vertical profiles of Z_H (Figure 5a), Z_{DR} (Figure 5b), and ρ_{hv} (Figure 5c) from SR1-P are displayed between 0200 and 1000 UTC 27 August over PIPS2A. The melting layer is located at 5 km as indicated by the bright-band in Z_H, enhanced positive Z_{DR} near 1.5 dB, and reduced ρ_{hv} ranging from 0.85 to 0.95 due to mixed-phase precipitation. From 0200 to 0400 UTC, Z_H was between 25 and 40 dBZ within the warm cloud layer and primarily decreased toward the surface below the melting layer. During this same time, Z_{DR} varied from 0.0 to 0.5 dB and exhibited little variation toward the surface below the melting layer. The combination of Z_H decreasing toward the surface and Z_{DR} remaining constant within the same layer translates to inferred dominant precipitation processes of evaporation and/or drop breakup (e.g., Carr et al., 2017; Porcacchia et al., 2019). During this time-frame, ρ_{hv} remained near 1.00 implying a rather uniform size distribution of drops (Herzegh & Jameson, 1992; Kumjian, 2013a; Ryzhkov, Giangrande, & Schuur, 2005; Ryzhkov, Schuur, et al., 2005; Zrnic & Ryzhkov, 1999).

From 0400 to 0730 UTC 27 August, near-surface Z_H increased to 35–50 dBZ (Figure 5a), whereas Z_{DR} also increased to 1.0–1.25 dB (Figure 5b). Further, both Z_H and Z_{DR} increased toward the surface for most of this period, translating to collision-coalescence dominant precipitation (Carr et al., 2017; Porcacchia et al., 2019), which occurred as the inner core (<100 km from TC center) moved over SR1-P from 0530 to 0800 UTC 27 August. There was also a slight upward displacement of the melting layer to 5.5–6.0 km from approximately 0330 UTC until 0800 UTC as latent heat release from convection in the inner core likely resulted in an increase in the height of the 0 C isotherm (Figure 5c). While K_{DP} generally ranged from 0.0 to 0.5°/km before 0400 UTC in the outer core and rainbands (Figure 5d), values of 1.0–2.0°/km were sampled below 2 km in the inner core and eyewall after 0500 UTC, implying a high number concentration of medium-sized drops as Z_{DR} ranged from 0.75 to 1.25 dB at this time.

3.2. GPM DPR Retrievals

The GPM DPR sampled Laura shortly before it made landfall on the southwest Louisiana coast at 0301 UTC 27 August (Figure 6). Figure 6 shows near-surface (just above ground level) KuPR, and vertical along-track cross-sections of KuPR, D_M, and $\log_{10}(N_w)$ through the inner core and eyewall. The southwestern and northeastern eyewall is characterized by echo top heights >12 km in the deepest convection, and also experienced an upward displacement of the 0 C isotherm to 6 km above the surface. This has been found to be associated with latent heat release in strong updrafts as higher θ_e air is transported from the boundary layer to the mid-troposphere (e.g., Fierro et al., 2012; Kirstetter et al., 2013; McGee & van den Heever, 2014). The cross-section illustrates KuPR of 50–55 dBZ in the eyewall with values ranging from 30 to 45 dBZ in regions of the outer core. D_M values of 2.0–2.5 mm occurred in the outer core at an along-track distance of 200–225 km, with lower values of 1.25–1.5 mm being observed in the eyewall. This differs from the location of maximum $\log_{10}(N_w)$ which occurred in the eyewall and exceeded 4.5 m^{-3} mm^{-1} within the deep convection, whereas the outer core had values between 2.75 and 3.5 m^{-3} mm^{-1}. This suggests that pre-landfall the eyewall had a large concentration of medium-sized drops, while the outer core had a PSD skewed toward smaller concentrations of larger drops. Another possibility for this abrupt transition between D_M and $\log_{10}(N_W)$ between the eyewall and outer core is a potential error in the DPR PSD algorithm. At an along-track distance of 70 km, the DPR estimated a D_M of 2.5–3.0 mm and $\log_{10}(N_W)$ values of 1–2 m^{-3} mm^{-1}, indicating a low concentration of large drops. One potential explanation for this feature is the presence of eyewall size-sorting, similar to how Laurencin et al. (2020) and Homeyer et al. (2021) observed offsets in maximum regions of Z_{DR} and K_{DP} using ground radar observations.

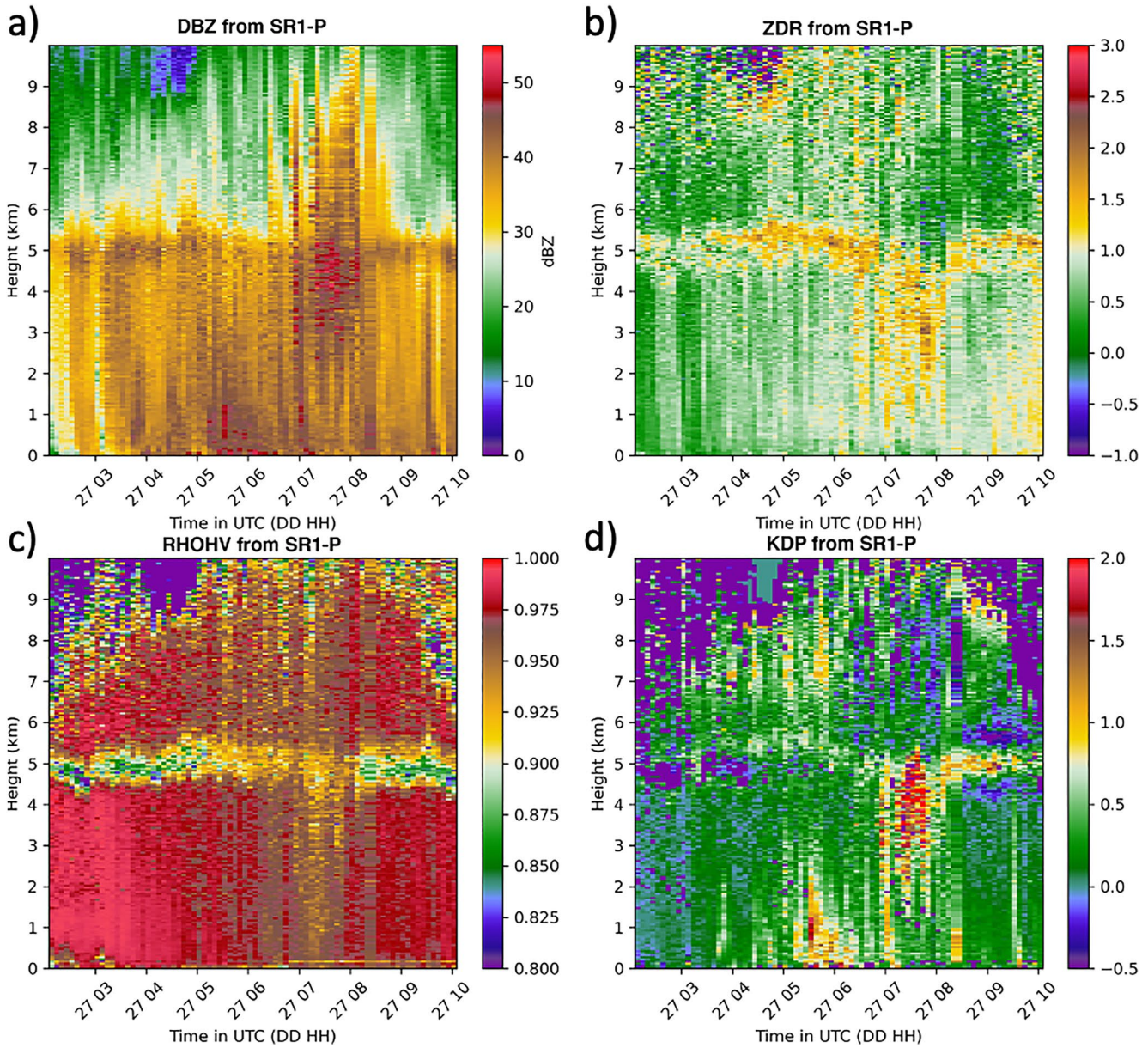

Figure 5. Columnar-vertical profiles (CVPs) of Z_H, Z_{DR}, ρ_{hv}, and K_{DP} from SR1-P from 0200 to 1000 UTC 27 August. Precipitation processes are inferred from the change in Z_H and Z_{DR} toward the surface below the melting layer, with increases toward the surface implying collision-coalescence.

The second DPR overpass occurred post-landfall at 1246 UTC 27 August as Laura tracked north over western Louisiana (Figure 7). Near-surface KuPR illustrates a broader inner core region with concentric spiral rainbands extending outward from the western portion of the center of circulation. The along-track cross-section through the rainbands shows cores of KuPR between 50–100 km and 150–175 km of 35–40 dBZ with a bright-band located between 4.5 and 5.0 km. Within the inner core at an along-track distance of 200–275 km, there was a slight increase in the 0 C isotherm to 5.5 km consistent with weaker convection compared to the pre-landfall case. A region of KuPR increasing toward the surface below 3 km can also be seen at an along-track distance of 250 km, inferring the presence of collision-coalescence processes (Porcacchia et al., 2019). At the same location an increase in D_M toward the surface can be seen which is collocated with maximum values of $\log_{10}(N_w)$ of 4.5 m^{-3} mm^{-1} implying the highest hydrometeor concentration in this region of the inner core. The constant values of $\log_{10}(N_w)$ with height at this location are likely non-physical and a product of the DPR PSD algorithm as it is known that drop concentration typically changes with height (Carr et al., 2017).

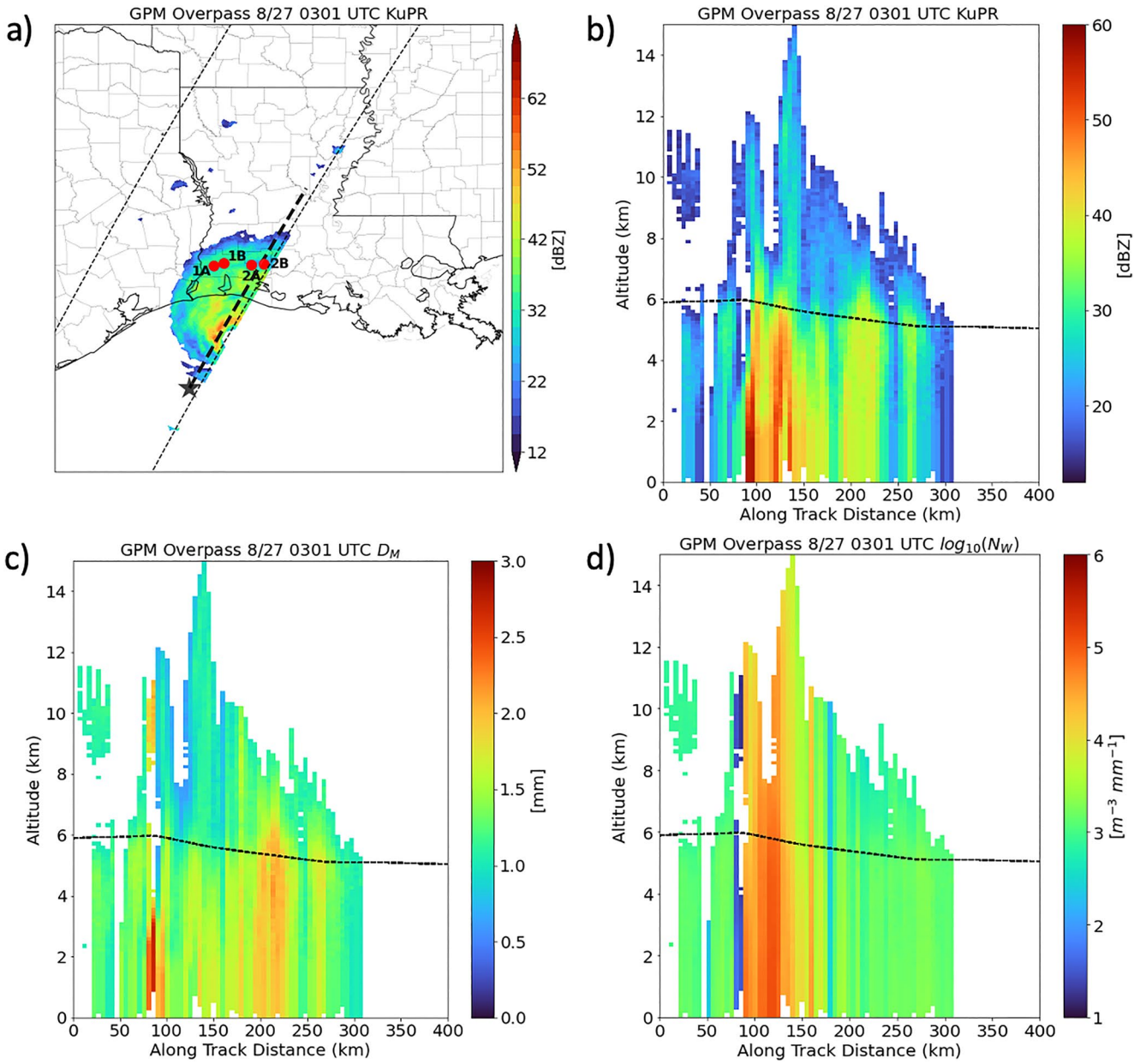

Figure 6. (a) Global precipitation measurement mission dual-frequency precipitation radar overpass at 0301 UTC 27 August (pre-landfall) showing attenuation-corrected near surface Ku-band reflectivity (KuPR) and portable in situ precipitation stations locations, (b) vertical profiles of KuPR, (c) mean drop diameter, and (d) normalized intercept parameter. Vertical cross-sections are taken along track from the star. The dashed black line represents the 0° C isotherm.

For the aforementioned along-track cross-sections, along-track vertical profiles of 25th, 50th, 75th, and 95th percentiles of KuPR were computed to identify and compare dominant precipitation processes before and after landfall (Figure 8). The first overpass contained more deep convective features as shown by the higher echo top heights for all percentiles. Further, there is a higher range of near-surface KuPR ranging from 23 to 50 dBZ at the surface, which is characteristic of convection. Pre-landfall, the region of enhanced KuPR located around the freezing level is deep ranging from 4.5 to 7.0 km which is anticipated in convection as updrafts loft mixed-phase hydrometeors vertically (e.g., Homeyer & Kumjian, 2015; Kirstetter et al., 2013; Loney et al., 2002). The post-landfall overpass illustrates a lower echo top height and a lower range in near-surface KuPR from 23 to 43 dBZ all indicating the presence of more stratiform precipitation.

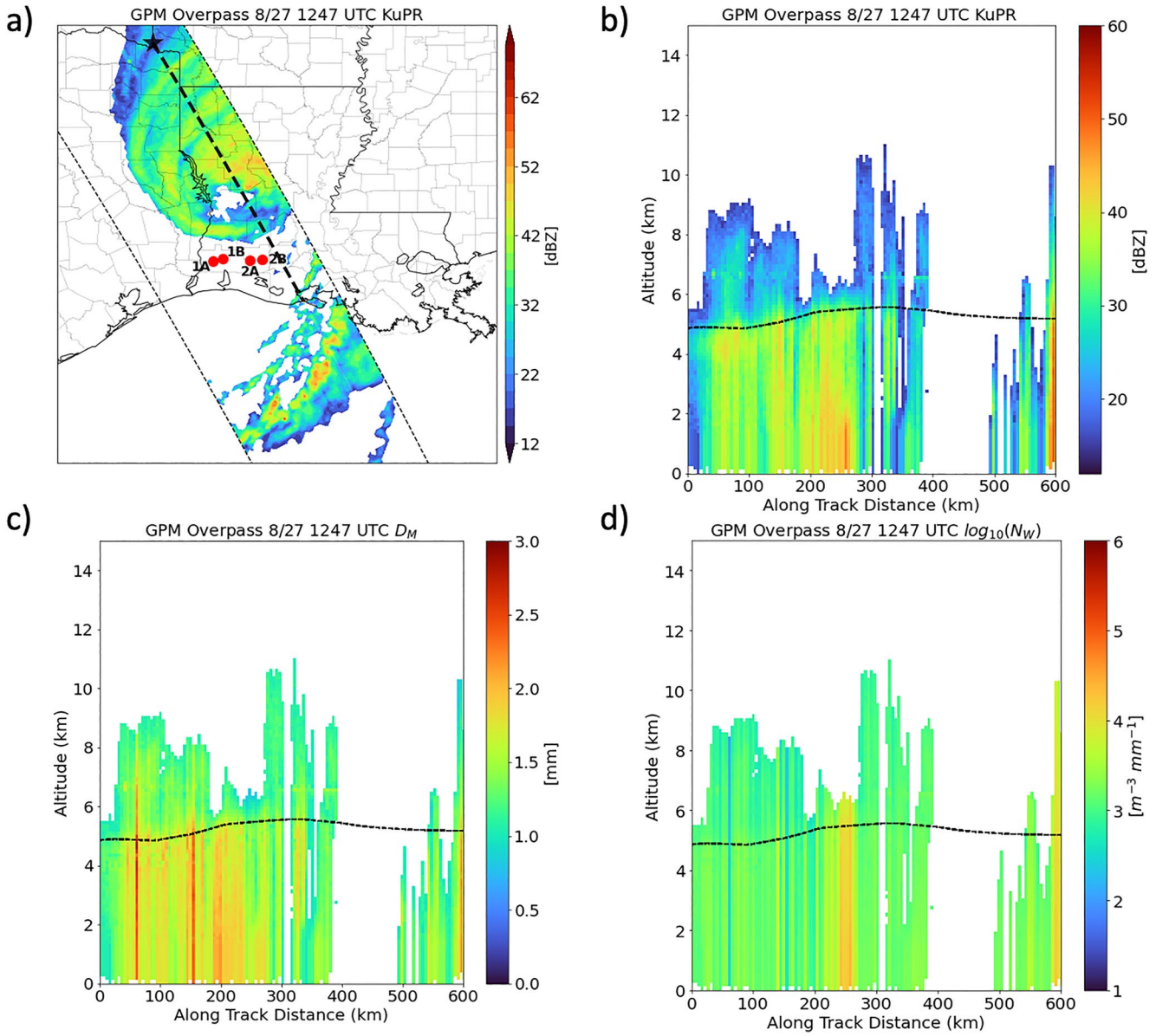

Figure 7. (a) Global precipitation measurement mission dual-frequency precipitation radar overpass at 1246 UTC 27 August (post-landfall) showing attenuation-corrected near surface Ku-band reflectivity (KuPR) and portable in situ precipitation stations locations, (b) vertical profiles of KuPR, (c) mean drop diameter, and (d) normalized intercept parameter. Vertical cross-sections are taken along track from the star. The dashed black line represents the 0° C isotherm.

Pre-landfall, the greater negative slope of the 95th and 75th KuPR percentiles between the freezing level and 2.5 km implies a higher magnitude of drop growth via collision-coalescence (Carr et al., 2017; Porcacchia et al., 2019) compared to the post-landfall overpass which illustrates a negative slope of lower magnitude, which is solely confined to the 95th percentile KuPR profile. The 25th percentile profile during this overpass shows a positive slope of KuPR below the melting layer, implying the presence of evaporation in less intense areas of precipitation, while more intense regions of precipitation (i.e., in convection) were dominated by collision-coalescence. The presence of vertical wind shear was unlikely the cause of the inferred evaporation post-landfall as 850-200 mb wind shear was less than 10 knots as Laura progressed inland (Figure 9), therefore disruption of the inner core likely occurred due to land interaction or dry air entrainment. The longwave 200 mb ridge pattern over the Gulf Coast region that contributed to this low-shear environment was favorable for Hurricane Laura to maintain major hurricane status up to and shortly after landfall.

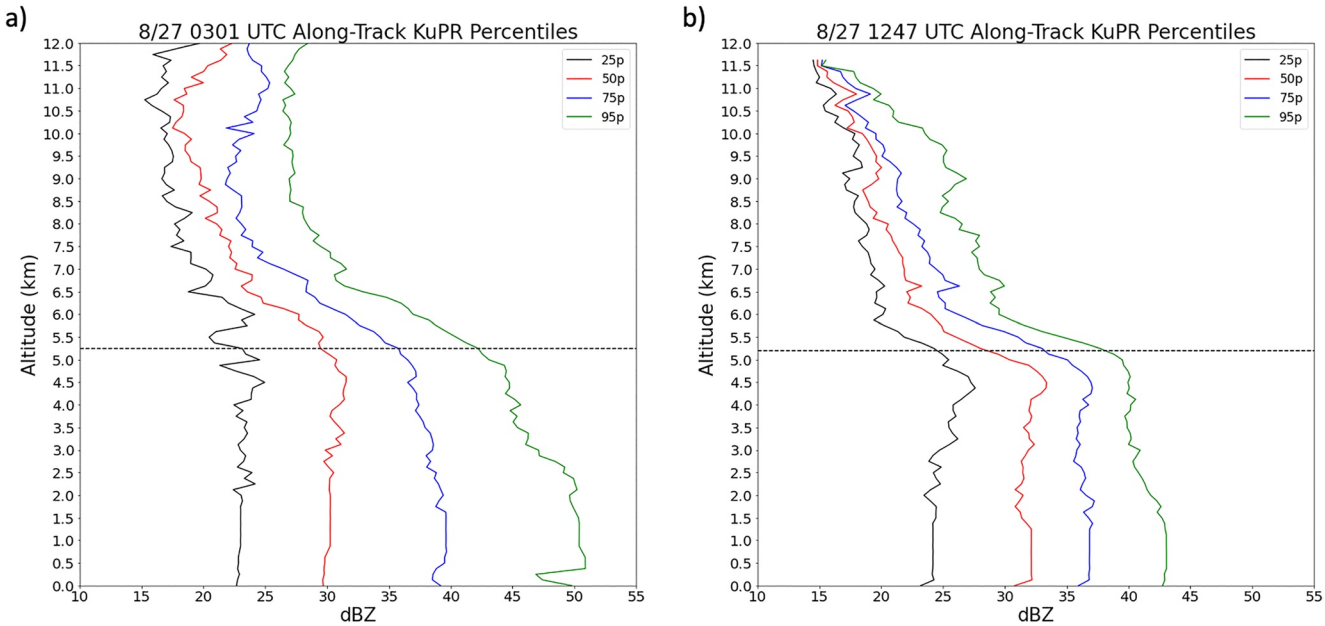

Figure 8. (a) Along-track percentiles of Ku-band reflectivity (KuPR) at 0301 UTC 27 August pre-landfall and (b) 1246 UTC 27 August post-landfall. The dashed line represents the along-track mean 0° C isotherm.

3.3. Disdrometer Observations

Figure 10 displays composite parsivel disdrometer observations of D_M and $\log_{10}(N_T)$ from PIPS 1A, PIPS 2A, and PIPS 2B between 2000 UTC 26 August and 1200 UTC 27 August. PIPS 1A experienced the western portion of the eyewall before becoming non-operational near 0700 UTC 27 August. $\log_{10}(N_T)$ ranged from 2.0 to 3.25 m^{-3}, corresponding to a D_M of 0.5–1.5 mm translating to a high concentration of small drops, particularly in the western portion of the inner core. The largest D_M (>2.0 mm) observed by PIPS 1A occurred as the spiral rainbands embedded in the outer core moved over the disdrometer after 0300 UTC.

PIPS 2A sampled the outer core from 0300 to 0530 UTC 27 August and primarily measured drop sizes below 1.5 mm, with the greatest $\log_{10}(N_T)$ of 2.0–2.5 m^{-3} occurring with D_M less than 1.0 mm. PIPS 2A observed a broader drop size distribution as the inner core moved over the station after 0525 UTC 27 August, with the largest values of $\log_{10}(N_T)$ near 3.0 m^{-3} occurring with drop sizes less than 1.0 mm, implying a high total concentration of small drops in the inner core and eastern eyewall. The outer periphery of the inner core was sampled by PIPS 2B after 0430 UTC 27 August, which measured the highest $\log_{10}(N_T)$ values of 3.0 m^{-3} coincident with a small drop size of 0.5–1.0 mm. Larger drops of 2.0–2.5 mm were observed at this time in the inner core, but at a lower total concentration of 1.5–2.0 m^{-3}. The drop size distribution was also much broader in the inner core compared to the outer core environment before 0330 UTC.

Figure 11 shows D_M gradually increasing from approximately 0.75 mm around 0100 UTC 27 August to near 1.5 mm at 0300 UTC 27 August as the outer core began to move over PIPS 1A. D_M then rapidly increased to values as high as 4.0 mm as the western portion of the inner core and eyewall moved over the disdrometer. This may be positively skewed toward a higher D_M as a broader drop size distribution was observed after the inner core moved over the observation site. PIPS 2A observed similar values of 0.5–1.5 mm in the outer core environment before measuring D_M values in the 1.0–4.0 mm range in the inner core, which is consistent with a broadening of the drop size distribution after the inner core moved over this disdrometer after 0530 UTC. PIPS 2B observed similar D_M values of 0.5–2.0 mm in the outer core increasing to values of 1.5–4.0 mm after 0430 UTC as the disdrometer began to sample the inner core. Figure 12 illustrates the time series of $\log_{10}(N_w)$ from each PIPS, and measured the values as high as 4.0 m^{-3} mm^{-1} in regions of the inner core and eyewall, while the outer core and outer rainbands were characterized by lower values ranging from 2.0 to 3.75 m^{-3} mm^{-1} implying a lower drop concentration.

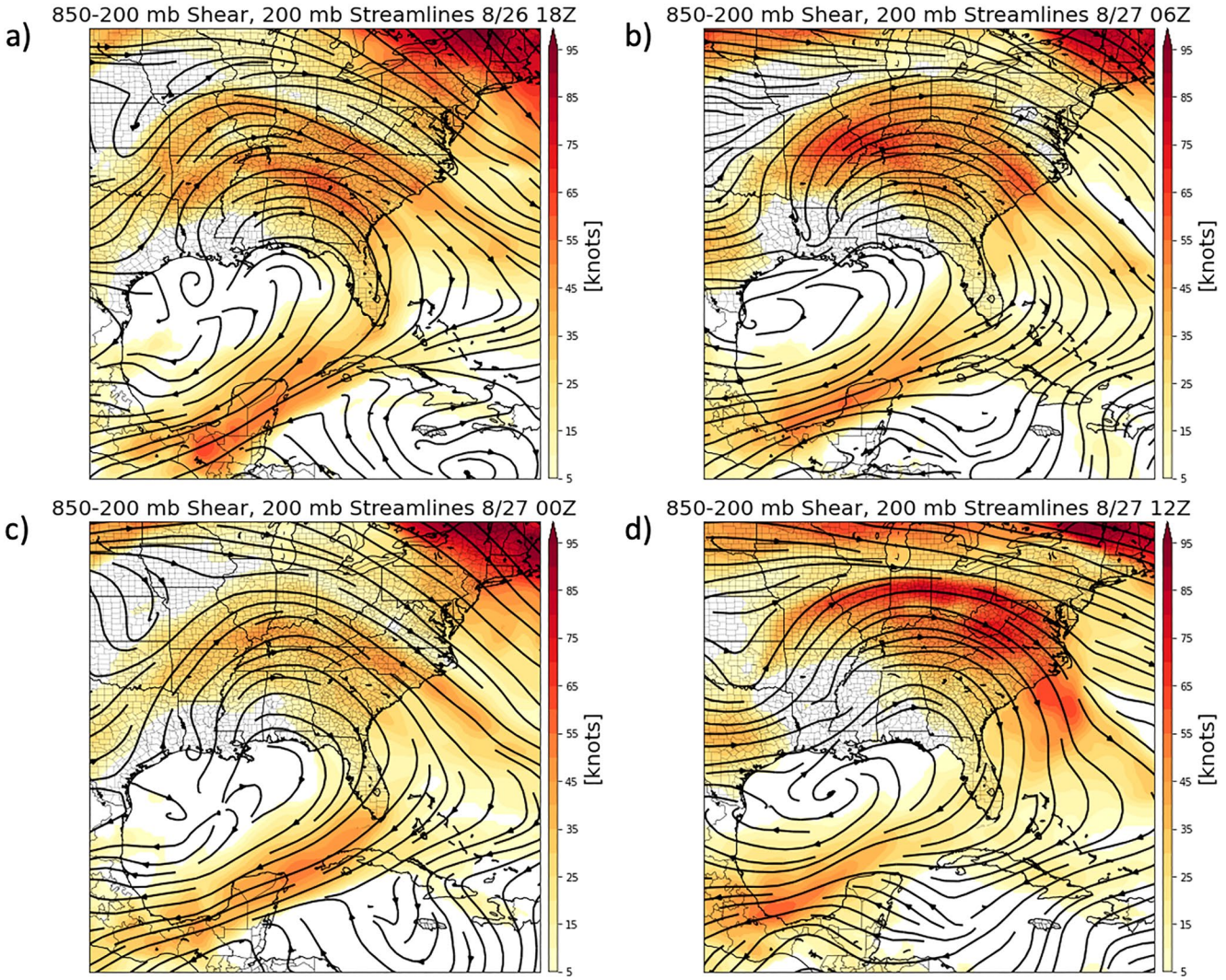

Figure 9. 850-200 mb environmental wind shear and 200 mb streamlines from 1800 UTC 26 August to 1200 UTC 27 August.

Z_H and Z_{DR} were derived from the PIPS PSD moments to provide a direct comparison with the SR1-P observations and the GPM DPR PSD algorithm (Figures 13 and 14). PIPS 1A observed Z_H values of 0–30 dBZ and Z_{DR} of 0–1 dB as it experienced the outer rainbands before 0300 UTC 27 August as it experienced periodic precipitation and a $D_M < 2.5$ mm. Z_H rapidly increased to 30–45 dBZ and Z_{DR} increased to 1–2 dB in the outer core after 0300 UTC, with the highest values of 50–60 dBZ (Z_H) and 1–2.5 dB (Z_{DR}) occurring in the western eyewall before 0700 UTC. PIPS 2A sampled a Z_H as high as 45 dBZ in the outer core of Laura before measuring peak values of 50–55 dBZ in the inner core and eyewall after 0530 UTC, with Z_{DR} increasing to 1–2.0 dB, indicating an increase in drop size. As PIPS 2B sampled the inner core, the highest Z_H values of 45–s55 dBZ were observed until 0730 UTC 27 August. However, the larger values of Z_{DR} from all PIPS may be positively biased by the larger drop sizes of 2.0–3.0 mm at a lower concentration that the disdrometer measured as Z_{DR} is independent of drop concentration (Kumjian, 2013a). Further, Z_H from SR1-P is higher than the estimated Z_H from PIPS 2B, which may be due to the radar sampling at a beam height of approximately 0.2 km over the disdrometer. One potential explanation for this difference is larger drops within the broader beam of the radar may not be sampled by the smaller footprint of PIPS 2B, whereas the low concentration of these larger drops acts to positively bias Z_H from SR1-P.

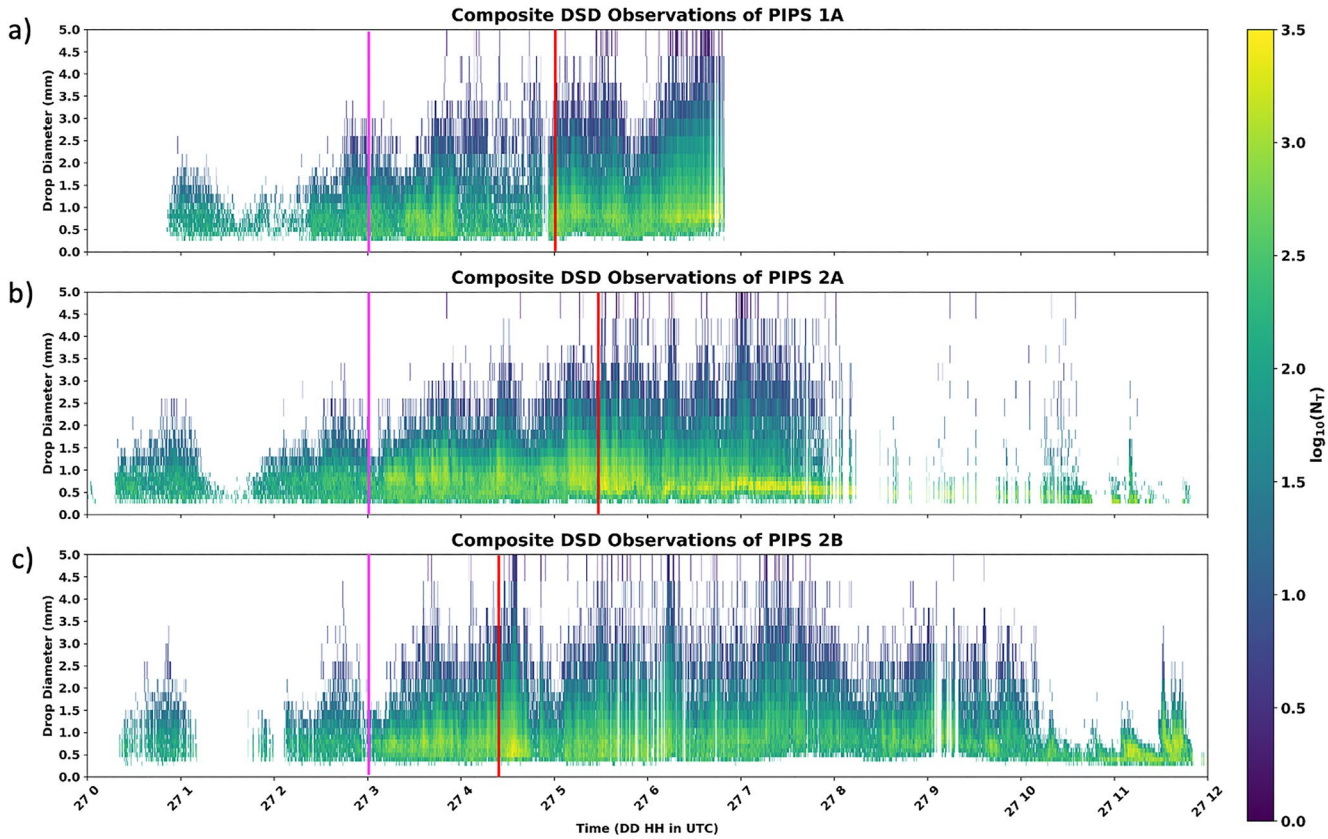

Figure 10. (a) Drop diameter and $\log_{10}(N_T)$ from portable in situ precipitation station 1A, (b) 2A, (c) and 2B from 2000 UTC 26 August to 1200 UTC 27 August. The red line represents the separation of the outer core from the inner core while the magenta line represents the time of the pre-landfall global precipitation measurement mission dual-frequency precipitation radar overpass (0301 UTC).

4. Discussion

Hurricane Laura provided a unique opportunity and novel data set to quantify drop size distribution characteristics in different portions of a landfalling TC using ground radar observations, space-borne radar retrievals, and disdrometer measurements. Prior research has examined the microphysical signatures in different regions of landfalling TCs using ground and space-borne radar observations (e.g., Brauer et al., 2021; DeHart & Bell, 2020; Didlake & Kumjian, 2017; Feng & Bell, 2019; Homeyer et al., 2021), however the use of disdrometer observations were not incorporated in order to verify PSD quantities and provide a direct comparison to estimations from remote sensing platforms as these retrievals were unavailable.

Ground radar observations from SR1-P exhibited the greatest increase in Z_H and Z_{DR} toward the surface below the melting layer from 0430 to 0700 UTC which are signatures of collision-coalescence dominant precipitation (e.g., Carr et al., 2017; Porcacchia et al., 2019). This occurred primarily in the inner core and western eyewall, and can be seen on both the composite RHI scans (Figures 4d and 4e) and CVPs (Figures 5a and 5b). Within the outer core and rainbands of Laura before 0330 UTC at the location of SR1-P, Z_H decreased with height below the melting layer while Z_{DR} increased slightly, which is consistent with evaporation and/or drop breakup (Figures 5a and 5b). The GPM DPR overpass at 0301 UTC 27 August shows KuPR and D_M increasing toward the surface in the eyewall at an along-track distance of 100–175 km which is indicative of collision-coalescence and/or a balance between collision-coalescence and drop breakup (Figures 6b and 6c). Further, in the region of the outer core at an along track distance of 200–300 km, KuPR remains constant below the 0 C isotherm, indicating the presence of evaporation or drop breakup (Figure 6b). PIPS 2B was located in proximity to the location of the along-track cross section from the DPR (Figure 6a), and measured a D_M near 1.5 mm at the time of the overpass. This value of D_M is similar to the 1.75 mm that the DPR algorithm extracted at an along-track distance of 260 km (Figure 6c). Further, the DPR algorithm estimated a $\log_{10}(N_W)$ value of 3.5 m^{-3} mm^{-1} at the same along-track distance which

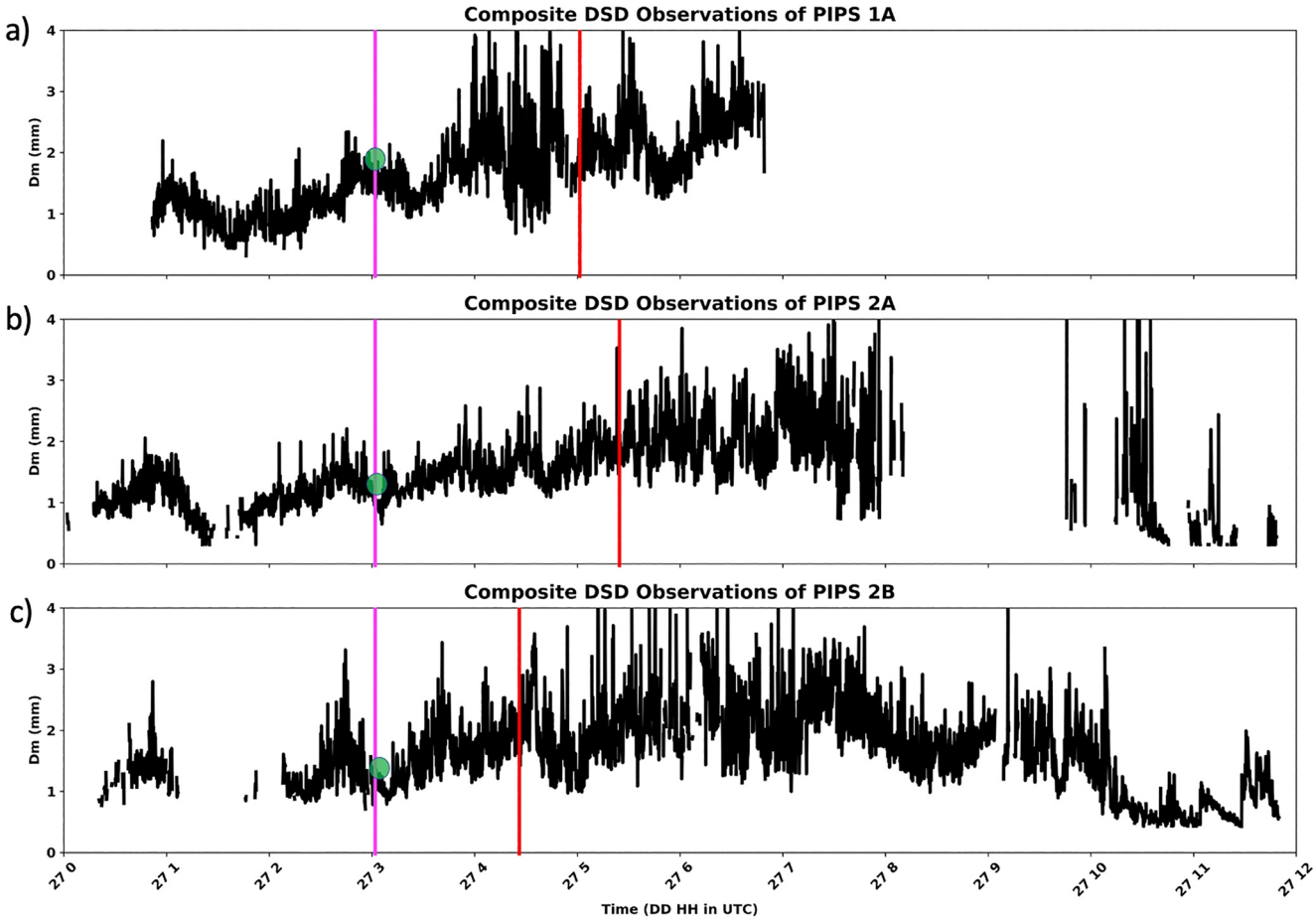

Figure 11. (a) D_M from portable in situ precipitation station 1A, (b) 2A, and (c) 2B from 2000 UTC 26 August to 1200 UTC 27 August. The red line represents the separation of the outer core from the inner core while the magenta line represents the time of the pre-landfall global precipitation measurement mission dual-frequency precipitation radar (GPM DPR) overpass (0301 UTC). The green circles represent the near-surface value of D_M from the pre-landfall GPM DPR overpass.

is higher than the $\log_{10}(N_T)$ value of 2.5–3.0 m^{-3} which was observed at the same drop size of 1.0 mm by the PIPS (Figures 6d and 10c), and temporally collocated with a $\log_{10}(N_W)$ value of 3.5 m^{-3} mm^{-1} estimated by the PIPS (Figure 12). This indicates that the DPR may be overestimating the drop number concentration in the outer core of Laura prior to landfall.

The post-landfall DPR overpass occurred at 1246 UTC 27 August (Figure 7), shortly after PIPS 2A and PIPS 2B stopped operating near 1200 UTC. During this time, the inner core of Laura had progressed inland, with both disdrometers being situated in the outer rainband environment. Figure 7b illustrates that KuPR is primarily constant toward the surface within the warm cloud layer outside of the inner core, with D_M ranging from 1.5 to 2.0 mm (Figure 7c) and $\log_{10}(N_W)$ near 3.5 m^{-3} mm^{-1} (Figure 7d). At an along-track distance of 200–260 km in the inner core, KuPR increased from 35 dBZ at 0° C isotherm, to 50 dBZ near the surface, implying collision-coalescence and/or a balance between collision-coalescence and drop breakup. D_M also increased from 1.25 to 1.50 mm near the melting layer, to 1.75–2.00 mm near the surface with the highest values of $\log_{10}(N_W)$ of 4.5 m^{-3} mm^{-1}. While the highest drop concentrations in the eyewall is consistent with prior studies (e.g., Didlake Jr. & Kumjian, 2018; Homeyer et al., 2021), the constant values of $\log_{10}(N_w)$ is likely a non-physical assumption of the DPR PSD algorithm as hydrometeor concentration is known to change with height through vertical profiles of Z_H and K_{DP} (e.g.,. Carr et al., 2017; Brauer et al., 2020). Figure 8 displays the comparison of KuPR percentiles from the pre-landfall overpass and the post-landfall overpass. At the 75th and 95th percentiles, the increase in KuPR toward the surface at 0301 UTC is greater than the slopes at 1246 UTC. This suggests that the magnitude of collision-coalescence dominant precipitation decreased from pre-landfall to post-landfall, which is also reflected in the smaller D_M values <1.0 mm after 0930 UTC 27 August that were observed by PIPS 2A and

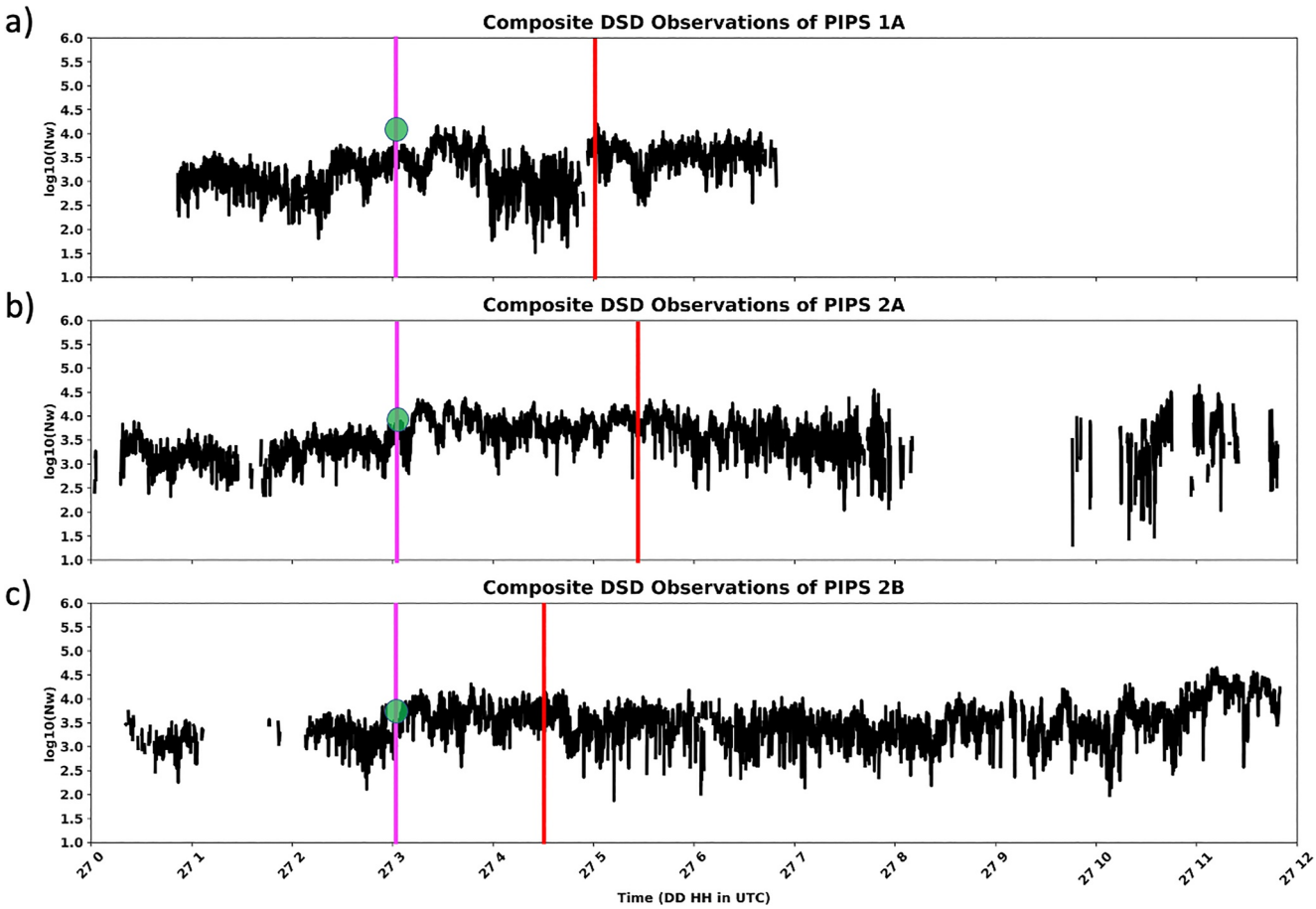

Figure 12. (a) $\log_{10}(N_w)$ from portable in situ precipitation station 1A, 2A (b), and 2B (c) from 2000 UTC 26 August to 1200 UTC 27 August. The red line represents the separation of the outer core from the inner core while the magenta line represents the time of the pre-landfall global precipitation measurement mission dual-frequency precipitation radar overpass (0301 UTC). The green circles represent the near-surface value of $\log_{10}(N_w)$ from the pre-landfall GPM DPR overpass.

PIPS 2B, indicating the increased presence of drop breakup or evaporation (i.e., non-CC processes). Further, the highest values of $\log_{10}(N_w)$ of 2.5–4.0 mm^{-3} occurred after 0900 UTC 27 August as well (Figure 12), which is consistent with a higher magnitude of drop breakup and/or a balanced between collision-coalescence and drop breakup, translating to a smaller mean drop size. While dominant precipitation processes in different portions of the storm are known to vary, both along-track cross-sections were computed through regions of the inner core and outer core, therefore the along-track percentiles of KuPR shown are consistent with showing a decrease in the frequency of collision-coalescence processes from pre-landfall to post-landfall (Figure 8).

While there are limitations when comparing observations of Z_H and Z_{DR} from disdrometers to ground radars (i.e., such as radar beam height increasing with range), disdrometers have been historically used to calibrate remote sensing platforms (e.g., Lee & Zawadzki, 2006; Martner, 1977). As PIPS 2A was close in proximity to SR1-P, a time series of Z_H and Z_{DR} from the ground radar provides a direct comparison between both observational platforms (Figures 13 and 14). As all PIPSs was located in the inner core and eyewall after 0530 UTC 27 August, the disdrometer observations estimated Z_H values of 35–50 dBZ, with the greatest values occurring from 0530 to 0730 UTC 27 August (Figure 13). Additionally, SR1-P observed lower values of Z_H by approximately 3–5 dBZ over PIPS 1A, potentially due to additional drop growth via collision-coalescence below radar beam height measured by the PIPS, especially in the inner core region after 0500 UTC. This difference may also be caused by the Z_H T-matrix calculation from the raw PSD retrievals.

A comparison of Z_{DR} between SR1-P and the PIPSs (Figure 14) illustrates additional differences. Z_{DR} initially ranged from 0.5 to 1.0 dB after 0330 UTC before increasing to as high as 1.5–2.0 dB at 0500 UTC in the inner core. These values are higher than SR1-P Z_{DR} values which primarily vary from 0.0 to 1.0 dB. The maximum

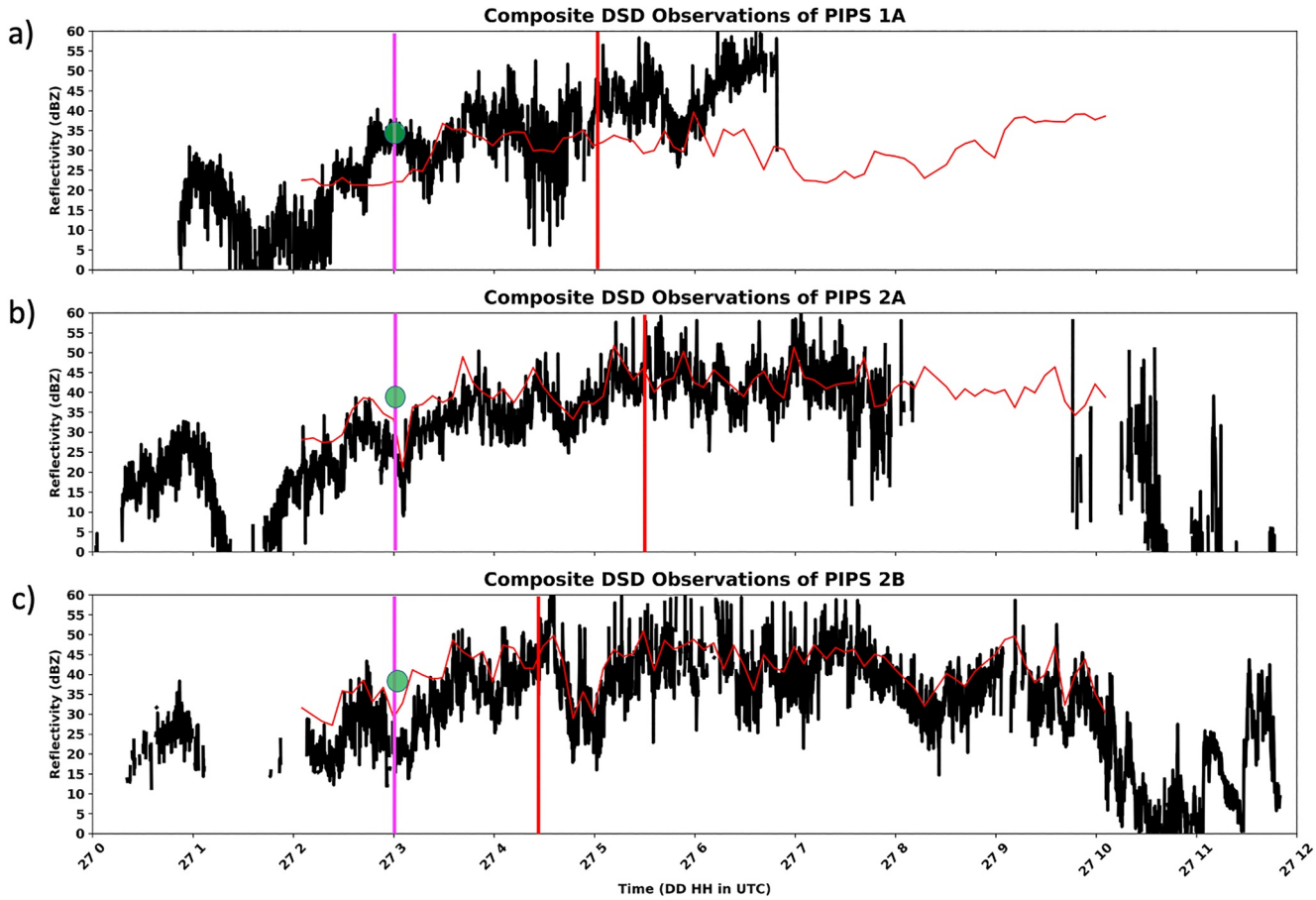

Figure 13. (a) Z_H from portable in situ precipitation station (PIPS) 1A, (b) 2A, and (c) 2B from 2000 UTC 26 August to 1200 UTC 27 August. The red line represents the separation of the outer core from the inner core while the magenta line represents the time of the pre-landfall global precipitation measurement mission dual-frequency precipitation radar (GPM DPR) overpass (0301 UTC). The green circles represents the near-surface value of Ku-band reflectivity (KuPR) from the pre-landfall GPM DPR overpass. The thin red line indicates Z_H from SR1-P over the location of each corresponding PIPS.

SR1-P Z_{DR} values of 0.5–1.5 dB occurred after 0500 UTC as SR1-P sampled the eyewall. As Z_{DR} is independent of number concentration, this negative bias from SR1-P may be caused by additional drop growth toward the surface as the beam height from SR1-P is approximately 900 m above the surface from PIPS 1A, 100 m above the surface from PIPS 2A, and 200 m above the surface from PIPS 2B. This is an additional source of uncertainty when computing Z_{DR} from the PIPS observations.

5. Conclusions

The mobile ground-radar observations, two GPM DPR overpasses, and three disdrometers were able to sample Hurricane Laura before, during, and after landfall as it impacted southwestern Louisiana from 26 to 27 August 2020. Both SR1-P and the GPM DPR observed signatures associated with collision-coalescence before and during landfall, with Z_H, Z_{DR}, and KuPR all increasing toward the surface below the melting layer which is indicative of drop growth. The PIPS observed a gradual increase in drop size up to landfall as the inner core moved onshore, as D_M increased from 1.0 mm to as high as 4.0 mm in the eyewall, with values decreasing to below 1.0 mm post-landfall. The GPM DPR observed similar signatures of the magnitude of collision-coalescence decreasing from pre-landfall to post-landfall, with a decreasingly negative slope of KuPR at the 95th percentile within the warm cloud layer toward the surface, implying an increased presence of drop breakup between both overpasses. Additionally, the larger range in KuPR indicates that more convection was present in the pre-landfall overpass, whereas the post-landfall DPR overpass illustrated the presence of more stratiform precipitation with some embedded convection. It was also found that prior to landfall, the DPR algorithm may be overestimating

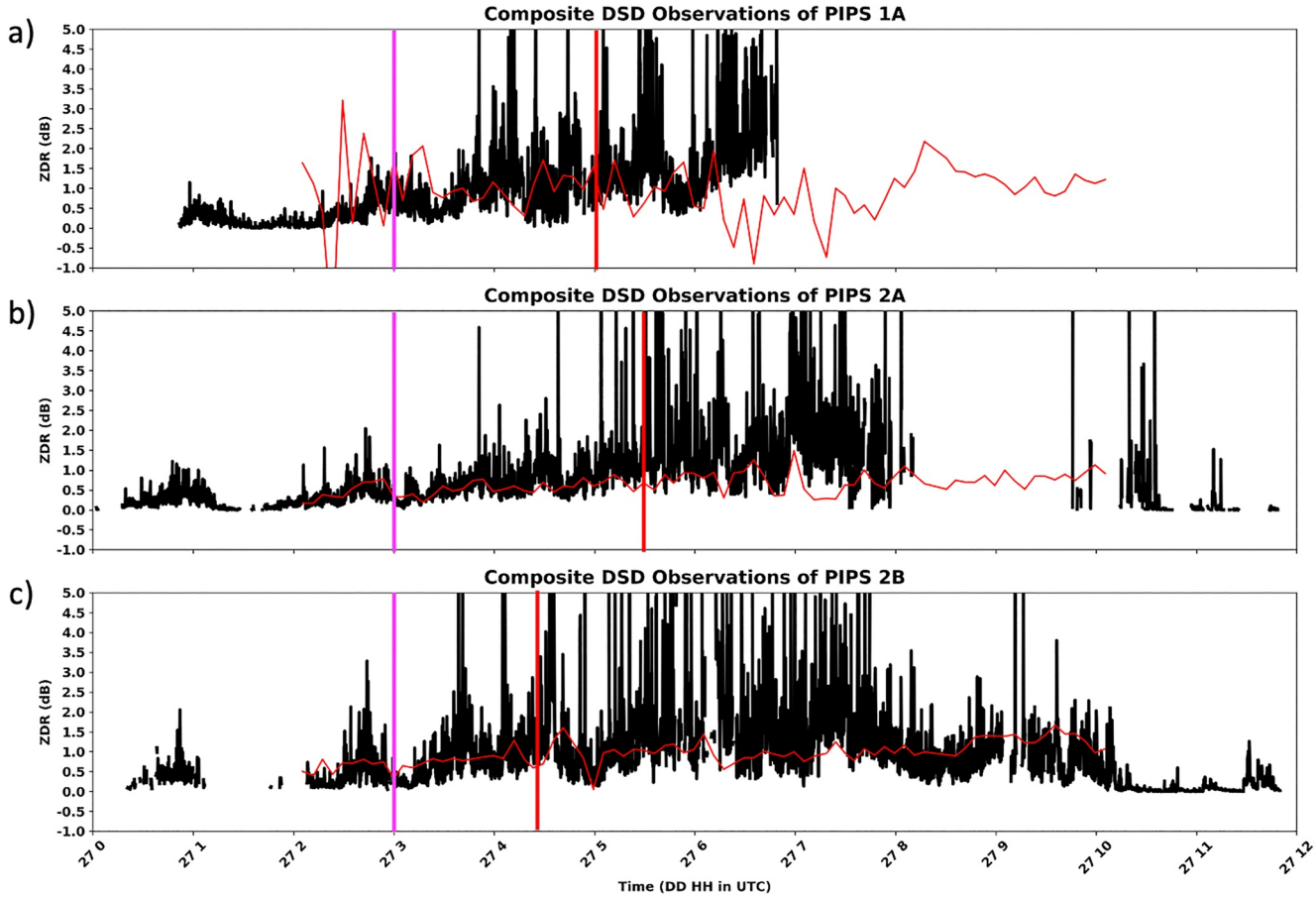

Figure 14. Z_{DR} from portable in situ precipitation station (PIPS) 1A, 2A, and 2B from 2000 UTC 26 August to 1200 UTC 27 August. The red line represents the separation of the outer core from the inner core while the magenta line represents the time of the pre-landfall global precipitation measurement mission dual-frequency precipitation radar overpass (0301 UTC). The thin red line indicates Z_{DR} from SR1-P over the location of each corresponding PIPS.

$\log_{10}(N_W)$ by 0.5–1.0 m^{-3} mm^{-1} in comparison to the PIPS, resulting in differences in drop number concentration between both retrieval methods. These results are similar to prior work from Huang et al. (2021) who compared DPR retrievals to disdrometer observations during the summer monsoon season in China. One potential reason for the DPR PSD algorithm overestimating $\log_{10}(N_w)$ compared to the PIPS is that the near-surface retrievals have been corrected for attenuation (https://www.eorc.jaxa.jp/GPM/doc/algorithm/ATBD_DPR_V07A.pdf). Future work can use disdrometer observations to correct for this assumption made by the DPR PSD algorithm to more accurately quantify D_M and $\log_{10}(N_W)$ at the surface in TCs. Lastly, Z_H and Z_{DR} from the PIPS were larger than the SR1-P retrievals, which may be due to additional drop growth via collision-coalescence below radar beam height.

Although it is a challenging task to deploy a mobile radar and multiple disdrometers in a landfalling TC, future studies should examine similar observations from all retrieval methods in order to determine if similar differences and similarities exist in TCs between ground radars, space-borne radar, and disdrometers to obtain a larger sample size. Further, one could incorporate S-band radar observations if available, as the KLCH WSR-88D become non-operational shortly before landfall. One additional avenue for future work would be to quantify and compare the derived rainfall rates using the polarimetric ground radar observations, the DPR-derived surface rainfall rate, and precipitation rates derived from the PIPS retrievals. This work can also be used to improve the DPR PSD algorithm, particularly in TCs. An additional limitation of this study is that each retrieval method sampled different portions of the TC at different times, therefore a denser observation network would be ideal to collect observation at different locations to provide a more detailed sample of different drop size distribution moments.

Data Availability Statement

The WSR-88D Level II polarimetric radar data used in this study can be accessed at https://www.ncdc.noaa.gov/nexradinv/ (Radar Operations Center, 2021). The SR1-P and PIPS data used in this study are accessible via https://zenodo.org/record/5518199#.YvWF_OzMLjA (N. Brauer et al., 2021). The GPM DPR data used in this work can be found at https://search.earthdata.nasa.gov/search?fp=GPM%26fi=DPR (Huffman et al., 2014). The ERA-5 reanalysis data set are openly available at https://cds.climate.copernicus.eu/cdsapp%23%21/dataset/reanalysis%2Dera5%2Dpressure%2Dlevels%3Ftab%3Dform (Hersbach et al., 2020). Figures were made using Matplotlib version 3.3.2 (Hunter, 2007).

Acknowledgments
Funding for this study was provided by the Future Investigators in NASA Earth Space Science and Technology (FINESST) award no. 80NSSC21K1637 which made this work possible. Pierre Kirstetter acknowledges support through the NASA Precipitation Measurement Missions award no. 80NSSC19K0681 and the NASA Ground Validation Program award no. NNX16AL23G. The radar and PIPS data collection was supported by the National Institute for Standards and Technology under award 70 NANB19H056. The authors also thank the three anonymous reviewers for providing constructive feedback to improve the quality of this study.

References

Atlas, D., Srivastava, R. C., & Sekhon, R. S. (1973). Doppler radar characteristics of precipitation at vertical incidence. *Reviews of Geophysics*, *11*(1), 1–35. https://doi.org/10.1029/RG011i001p00001

Atlas, D., & Ulbrich, C. W. (2000). An observationally based conceptual model of warm oceanic convective rain in the tropics. *Journal of Applied Meteorology*, *39*(12), 2165–2181. https://doi.org/10.1175/1520-0450(2001)040<2165:aobcmo>2.0.co;2

Austin, P. M. (1987). Relation between measured radar reflectivity and surface rainfall. *Monthly Weather Review*, *115*(5), 1053–1070. https://doi.org/10.1175/1520-0493(1987)115<1053:rbmrra>2.0.co;2

Biggerstaff, M. I., Alford, A. A., Carrie, G. D., & Stevenson, J. A. (2021). Hurricane Florence (2018): Long duration single- and dual-Doppler observations and wind retrievals during landfall. *Geoscience Data Journal*. https://doi.org/10.1002/gdj3.137

Biggerstaff, M. I., Wicker, L. J., Guynes, J., Ziegler, C., Straka, J. M., Rasmussen, E. N., et al. (2005). The shared mobile atmospheric research and teaching radar: A collaboration to enhance research and teaching. *Bulletin of the American Meteorological Society*, *86*(9), 1263–1274. https://doi.org/10.1175/BAMS-86-9-1263

Brauer, N., Alford, A., Waugh, S., Biggerstaff, M., Carrie, G., Dawson, D., et al. (2021). Data archive for: Hurricane Laura (2020): A comparison of drop size distribution moments using ground and radar remote sensing retrieval methods [Dataset]. Zenodo. Retrieved from https://zenodo.org/record/5518199#.YvWF_OzMLjA

Brauer, N. S., Basara, J. B., Homeyer, C. R., McFarquhar, G. M., & Kirstetter, P. E. (2020). Quantifying precipitation efficiency and drivers of excessive precipitation in post-landfall Hurricane Harvey. *Journal of Hydrometeorology*, *21*(3), 433–452. https://doi.org/10.1175/JHM-D-19-0192.1

Brauer, N. S., Basara, J. B., Kirstetter, P. E., Wakefield, R. A., Homeyer, C. R., Yoo, J., et al. (2021). The inland maintenance and re-intensification of tropical Storm Bill (2015) Part 2: Precipitation microphysics. *Journal of Hydrometeorology*. https://doi.org/10.1175/JHM-D-20-0151.1

Cannon, F., Ralph, F. M., Wilson, A. M., & Lettenmaier, D. P. (2017). GPM satellite radar measurements of precipitation and freezing level in atmospheric rivers: Comparison with ground-based radars and reanalyses. *Journal of Geophysical Research: Atmospheres*, *122*(23), 12747–12764. https://doi.org/10.1002/2017JD027355

Carr, N., Kirstetter, P. E., Gourley, J. J., & Hong, Y. (2017). Polarimetric signatures of midlatitude warm-rain precipitation events. *Journal of Applied Meteorology and Climatology*, *56*(3), 697–711. https://doi.org/10.1175/JAMC-D-16-0164.1

Cecil, D. J., Zipser, E. J., & Nesbitt, S. W. (2002). Reflectivity, ice scattering, and lightning characteristics of hurricane eyewalls and rainbands. Part I: Quantitative description. *Monthly Weather Review*, *130*(4), 769–784. https://doi.org/10.1175/1520-0493(2002)130<0769:risalc>2.0.co;2

Chen, H., & Gopalakrishnan, S. (2014). A study on the asymmetric rapid intensification of Hurricane Earl (2010) using the HWRF system. *Journal of the Atmospheric Sciences*, *72*(2), 531–550. https://doi.org/10.1175/JAS-D-14-0097.1

Cressman, G. P. (1959). An operational objective analysis system. *Monthly Weather Review*, *87*(10), 367–374. https://doi.org/10.1175/1520-0493(1959)087<0367:aooas>2.0.co;2

Cunha, L. K., Smith, J. A., Baeck, M. L., & Krajewski, W. F. (2013). An early performance evaluation of the NEXRAD dual-polarization radar rainfall estimates for urban flood applications. *Weather and Forecasting*, *28*(6), 1478–1497. https://doi.org/10.1175/WAF-D-13-00046.1

Dawson, D., Biggerstaff, M., & Waugh, S. (2017). *Purdue University portable in situ precipitation stations (PIPS) data*. UCAR/NCAR - Earth Observing Laboratory. https://doi.org/10.5065/D6GB22R5

DeHart, J. C., & Bell, M. M. (2020). A comparison of the polarimetric radar characteristics of heavy rainfall from Hurricanes Harvey (2017) and Florence (2018). *Journal of Geophysical Research: Atmospheres*, *125*(11), e2019JD032212. https://doi.org/10.1029/2019JD032212

Didlake, A. C., & Kumjian, M. R. (2017). Examining polarimetric radar observations of bulk microphysical structures and their relation to vortex kinematics in Hurricane Arthur (2014). *Monthly Weather Review*, *145*(11), 4521–4541. https://doi.org/10.1175/MWR-D-17-0035.1

Didlake, A. C., Jr., & Kumjian, M. R. (2018). Examining storm asymmetries in Hurricane Irma (2017) using polarimetric radar observations. *Geophysical Research Letters*, *45*(24), 13513–13522. https://doi.org/10.1029/2018GL080739

Feng, Y.-C., & Bell, M. M. (2019). Microphysical characteristics of an asymmetric eyewall in major Hurricane Harvey (2017). *Geophysical Research Letters*, *46*(1), 461–471. https://doi.org/10.1029/2018GL080770

Fierro, A. O., Zipser, E. J., LeMone, M. A., Straka, J. M., & Simpson, J. M. (2012). Tropical oceanic hot towers: Need they be undilute to transport energy from the boundary layer to the upper troposphere effectively? An answer based on trajectory analysis of a simulation of a TOGA COARE convective system. *Journal of the Atmospheric Sciences*, *69*(1), 195–213. https://doi.org/10.1175/JAS-D-11-0147.1

Friedrich, K., Higgins, S., Masters, F. J., & Lopez, C. R. (2013). Articulating and stationary PARSIVEL disdrometer measurements in conditions with strong winds and heavy rainfall. *Journal of Atmospheric and Oceanic Technology*, *30*(9), 2063–2080. https://doi.org/10.1175/JTECH-D-12-00254.1

Giangrande, S. E., Krause, J. M., & Ryzhkov, A. (2008). Automatic designation of the melting layer with a polarimetric prototype of the WSR-88d radar. *Journal of Applied Meteorology and Climatology*, *47*(5), 1354–1364. https://doi.org/10.1175/2007JAMC1634.1

Gorgucci, E., Scarchilli, G., & Chandrasekar, V. (1992). Calibration of radars using polarimetric techniques. *IEEE Transactions on Geoscience and Remote Sensing*, *30*(5), 853–858. https://doi.org/10.1109/36.175319

Hersbach, H., Bell, B., Berrisford, P., Hirahara, S., Horányi, A., Muñoz-Sabater, J., et al. (2020). The ERA5 global reanalysis [Dataset]. [Accessed 3 March 2021]. Quarterly Journal of the Royal Meteorological Society, *146*(730), 1999–2049. https://doi.org/10.1002/qj.3803

Herzegh, P. H., & Jameson, A. R. (1992). Observing precipitation through dual-polarization radar measurements. *Bulletin of the American Meteorological Society*, *73*(9), 1365–1376. https://doi.org/10.1175/1520-0477(1992)073<1365:optdpr>2.0.co;2

Homeyer, C. R., Fierro, A. O., Schenkel, B. A., Didlake, A. C., McFarquhar, G. M., Hu, J., et al. (2021). Polarimetric signatures in landfalling tropical cyclones. *Monthly Weather Review*, *149*(1), 131–154. https://doi.org/10.1175/MWR-D-20-0111.1

Homeyer, C. R., & Kumjian, M. R. (2015). Microphysical characteristics of overshooting convection from polarimetric radar observations. *Journal of the Atmospheric Sciences*, *72*(2), 870–891. https://doi.org/10.1175/JAS-D-13-0388.1

Hou, A. Y., Kakar, R. K., Neeck, S., Azarbarzin, A. A., Kummerow, C. D., Kojima, M., et al. (2014). The global precipitation measurement mission. *Bulletin of the American Meteorological Society*, *95*(5), 701–722. https://doi.org/10.1175/BAMS-D-13-00164.1

Hristova-Veleva, S., Haddad, Z., Chau, A., Stiles, B. W., Turk, F. J., Li, P. P., et al. (2021). Impact of microphysical parameterizations on simulated hurricanes—Using multi-parameter satellite data to determine the particle size distributions that produce most realistic storms. *Atmosphere*, *12*(2), 154. https://doi.org/10.3390/atmos12020154

Huang, C., Chen, S., Zhang, A., & Pang, Y. (2021). Statistical characteristics of raindrop size distribution in monsoon season over South China Sea. *Remote Sensing*, *13*(15), 2878. https://doi.org/10.3390/rs13152878

Huang, H., & Chen, F. (2019). Precipitation microphysics of tropical cyclones over the Western North Pacific based on GPM DPR observations: A preliminary analysis. *Journal of Geophysical Research: Atmospheres*, *124*(6), 3124–3142. https://doi.org/10.1029/2018JD029454

Huffman, G., Bolvin, D., Braithwaite, D., Hsu, K., Joyce, R., & Xie, P. (2014). Integrated multi-satellite retrievals for GPM (IMERG), version 4.4 [Dataset]. Arthurhou. [Accessed 3 March 2021]. Retrieved from ftp://arthurhou.pps.eosdis.nasa.gov/gpmdata/

Hunter, J. D. (2007). Matplotlib: A 2D graphics environment [software]. Computing in Science & Engineering, *9*(3), 90–95. https://doi.org/10.1109/MCSE.2007.55

Jameson, A. R. (1985). Microphysical interpretation of multiparameter radar measurements in rain. Part III: Interpretation and measurement of propagation differential phase shift between orthogonal linear polarizations. *Journal of the Atmospheric Sciences*, *42*(6), 607–614. https://doi.org/10.1175/1520-0469(1985)042<0607:miomrm>2.0.co;2

Jiang, H., Liu, C., & Zipser, E. J. (2011). A TRMM-based tropical cyclone cloud and precipitation feature database. *Journal of Applied Meteorology and Climatology*, *50*(6), 1255–1274. https://doi.org/10.1175/2011JAMC2662.1

Jorgensen, D. P., & Willis, P. T. (1982). A z-r relationship for hurricanes. *Journal of Applied Meteorology and Climatology*, *21*(3), 356–366. https://doi.org/10.1175/1520-0450(1982)021<0356:azrrfh>2.0.co;2

Kalina, E. A., Friedrich, K., Ellis, S. M., & Burgess, D. W. (2014). Comparison of disdrometer and x-band mobile radar observations in convective precipitation. *Monthly Weather Review*, *142*(7), 2414–2435. https://doi.org/10.1175/MWR-D-14-00039.1

Kirstetter, P.-E., Andrieu, H., Boudevillain, B., & Delrieu, G. (2013). A physically based identification of vertical profiles of reflectivity from volume scan radar data. *Journal of Applied Meteorology and Climatology*, *52*(7), 1645–1663. https://doi.org/10.1175/JAMC-D-12-0228.1

Kumjian, M. (2013a). Principles and applications of dual-polarization weather radar. Part I: Description of the polarimetric radar variables. *Journal of Operational Meteorology*, *1*(19), 226–242. https://doi.org/10.15191/nwajom.2013.0119

Kumjian, M. (2013b). Principles and applications of dual-polarization weather radar. Part II: Warm- and cold-season applications. *Journal of Operational Meteorology*, *1*(20), 243–264. https://doi.org/10.15191/nwajom.2013.0120

Kumjian, M., & Ryzhkov, A. (2012). The impact of size sorting on the polarimetric radar variables. *Journal of the Atmospheric Sciences*, *69*(6), 2042–2060. https://doi.org/10.1175/jas-d-11-0125.1

Kummerow, C., Barnes, W., Kozu, T., Shiue, J., & Simpson, J. (1998). The tropical rainfall measuring mission (TRMM) sensor package. *Journal of Atmospheric and Oceanic Technology*, *15*(3), 809–817. https://doi.org/10.1175/1520-0426(1998)015<0809:ttrmmt>2.0.co;2

Laurencin, C. N., Didlake, A. C., Jr., Loeffler, S. D., Kumjian, M. R., & Heymsfield, G. M. (2020). Hydrometeor size sorting in the asymmetric eyewall of Hurricane Matthew (2016). *Journal of Geophysical Research: Atmospheres*, *125*(17), e2020JD032671. https://doi.org/10.1029/2020JD032671

Lee, G., & Zawadzki, I. (2006). Radar calibration by gage, disdrometer, and polarimetry: Theoretical limit caused by the variability of drop size distribution and application to fast scanning operational radar data. *Journal of Hydrology*, *328*(1–2), 83–97. https://doi.org/10.1016/j.jhydrol.2005.11.046

Liao, L., & Meneghini, R. (2019). Physical evaluation of GPM DPR single- and dual-wavelength algorithms. *Journal of Atmospheric and Oceanic Technology*, *36*(5), 883–902. https://doi.org/10.1175/JTECH-D-18-0210.1

Liao, L., Meneghini, R., & Tokay, A. (2014). Uncertainties of GPM DPR rain estimates caused by DSD parameterizations. *Journal of Applied Meteorology and Climatology*, *53*(11), 2524–2537. https://doi.org/10.1175/JAMC-D-14-0003.1

List, R., Donaldson, N. R., & Stewart, R. E. (1987). Temporal evolution of drop spectra to collisional equilibrium in steady and pulsating rain. *Journal of the Atmospheric Sciences*, *44*(2), 362–372. https://doi.org/10.1175/1520-0469(1987)044<0362:teodst>2.0.co;2

Loney, M. L., Zrnić, D. S., Straka, J. M., & Ryzhkov, A. V. (2002). Enhanced polarimetric radar signatures above the melting level in a supercell storm. *Journal of Applied Meteorology*, *41*(12), 1179–1194. https://doi.org/10.1175/1520-0450(2002)041<1179:eprsat>2.0.co;2

Marra, A. C., Federico, S., Montopoli, M., Avolio, E., Baldini, L., Casella, D., et al. (2019). The precipitation structure of the mediterranean tropical-like cyclone NUMA: Analysis of GPM observations and numerical weather prediction model simulations. *Remote Sensing*, *11*(14), 1690. https://doi.org/10.3390/rs11141690

Martner, B. E. (1977). A field experiment on the calibration of radars with raindrop disdrometers. *Journal of Applied Meteorology*, *16*(4), 451–454. https://doi.org/10.1175/1520-0450(1977)016<0451:afeotc>2.0.co;2

McFarquhar, G. M., & Black, R. A. (2004). Observations of particle size and phase in tropical cyclones: Implications for mesoscale modeling of microphysical processes. *Journal of the Atmospheric Sciences*, *61*(4), 422–439. https://doi.org/10.1175/1520-0469(2004)061<0422:oopsap>2.0.co;2

McGee, C. J., & van den Heever, S. C. (2014). Latent heating and mixing due to entrainment in tropical deep convection. *Journal of the Atmospheric Sciences*, *71*(2), 816–832. https://doi.org/10.1175/JAS-D-13-0140.1

Medlin, J. M., Kimball, S. K., & Blackwell, K. G. (2007). Radar and rain gauge analysis of the extreme rainfall during Hurricane Danny's (1997) landfall. *Monthly Weather Review*, *135*(5), 1869–1888. https://doi.org/10.1175/MWR3368.1

Meneghini, R., Kim, H., Liao, L., Jones, J. A., & Kwiatkowski, J. M. (2015). An initial assessment of the surface reference technique applied to data from the dual-frequency precipitation radar (DPR) on the GPM Satellite. *Journal of Atmospheric and Oceanic Technology*, *32*(12), 2281–2296. https://doi.org/10.1175/JTECH-D-15-0044.1

Merceret, F. J. (1974). On the size distribution of raindrops in hurricane ginger. *Monthly Weather Review*, *102*(10), 714–716. https://doi.org/10.1175/1520-0493(1974)102<0714:otsdor>2.0.co;2

Murphy, A. M., Ryzhkov, A., & Zhang, P. (2020). Columnar vertical profile (CVP) methodology for validating polarimetric radar retrievals in ice using in situ aircraft measurements. *Journal of Atmospheric and Oceanic Technology*, *37*(9), 1623–1642. https://doi.org/10.1175/JTECH-D-20-0011.1

National Hurricane Center. (2021). *National hurricane center tropical cyclone report: Hurricane Laura*. National Hurricane Center. Retrieved from https://www.nhc.noaa.gov/data/tcr/AL132020_Laura.pdf

Park, S.-G., Kim, H.-L., Ham, Y.-W., & Jung, S.-H. (2017). Comparative evaluation of the OTT PARSIVEL2 using a collocated two-dimensional video disdrometer. *Journal of Atmospheric and Oceanic Technology*, *34*(9), 2059–2082. https://doi.org/10.1175/JTECH-D-16-0256.1

Porcacchia, L., Kirstetter, P.-E., Maggioni, V., & Tanelli, S. (2019). Investigating the GPM dual-frequency precipitation radar signatures of low-level precipitation enhancement. *Quarterly Journal of the Royal Meteorological Society*, *145*(724), 3161–3174. https://doi.org/10.1002/qj.3611

Radar Operations Center, N. U. D. O. C., National Weather Service. (2021). NOAA national weather service (NWS) radar operations center (1991): NOAA next generation radar (NEXRAD) level 2 base data [Dataset]. NCDC. https://doi.org/10.7289/V5W9574V [Accessed 3 March 2021]. Retrieved from https://www.ncdc.noaa.gov/nexradinv/

Radhakrishna, B., Satheesh, S. K., Narayana Rao, T., Saikranthi, K., & Sunilkumar, K. (2016). Assessment of DSDS of GPM-DPR with ground-based disdrometer at seasonal scale over Gadanki, India. *Journal of Geophysical Research: Atmospheres*, *121*(19), 11792–11802. https://doi.org/10.1002/2015JD024628

Rappaport, E. N. (2000). Loss of life in the United States associated with recent Atlantic tropical cyclones. *Bulletin of the American Meteorological Society*, *81*(9), 2065–2074. https://doi.org/10.1175/1520-0477(2000)081<2065:lolitu>2.3.co;2

Rappaport, E. N. (2014). Fatalities in the United States from Atlantic tropical cyclones: New data and interpretation. *Bulletin of the American Meteorological Society*, *95*(3), 341–346. https://doi.org/10.1175/BAMS-D-12-00074.1

Ryzhkov, A. (2007). The impact of beam broadening on the quality of radar polarimetric data. *Journal of Atmospheric and Oceanic Technology*, *24*(5), 729–744. https://doi.org/10.1175/JTECH2003.1

Ryzhkov, A., Giangrande, S. E., Melnikov, V. M., & Schuur, T. J. (2005). Calibration issues of dual-polarization radar measurements. *Journal of Atmospheric and Oceanic Technology*, *22*(8), 1138–1155. https://doi.org/10.1175/JTECH1772.1

Ryzhkov, A., Giangrande, S. E., & Schuur, T. J. (2005). Rainfall estimation with a polarimetric prototype of WSR-88d. *Journal of Applied Meteorology*, *44*(4), 502–515. https://doi.org/10.1175/JAM2213.1

Ryzhkov, A., Schuur, T. J., Burgess, D. W., Heinselman, P. L., Giangrande, S. E., & Zrnic, D. S. (2005). The joint polarization experiment: Polarimetric rainfall measurements and hydrometeor classification. *Bulletin of the American Meteorological Society*, *86*(6), 809–824. https://doi.org/10.1175/BAMS-86-6-809

Ryzhkov, A., Zhang, P., Reeves, H., Kumjian, M., Tschallener, T., Trömel, S., & Simmer, C. (2016). Quasi-vertical profiles—A new way to look at polarimetric radar data. *Journal of Atmospheric and Oceanic Technology*, *33*(3), 551–562. https://doi.org/10.1175/JTECH-D-15-0020.1

Sanchez-Rivas, D., & Rico-Ramirez, M. (2021). Calibration of radar differential reflectivity using Quasi-vertical profiles. *Atmospheric Measurement Techniques*. https://doi.org/10.5194/amt-2021-194

Science Applications International Corporation and National Hurricane Center (1993). *Global tropical cyclone "best track" position and intensity data*. Research Data Archive at the National Center for Atmospheric Research, Computational and Information Systems Laboratory. Retrieved from http://rda.ucar.edu/datasets/ds824.1/

Seliga, T. A., & Bringi, V. N. (1976). Potential use of radar differential reflectivity measurements at orthogonal polarizations for measuring precipitation. *Journal of Applied Meteorology*, *15*(1), 69–76. https://doi.org/10.1175/1520-0450(1976)015<0069:puordr>2.0.co;2

Seliga, T. A., & Bringi, V. N. (1978). Differential reflectivity and differential phase shift: Applications in radar meteorology. *Radio Science*, *13*(2), 271–275. https://doi.org/10.1029/RS013i002p00271

Sheppard, B. E., & Joe, P. I. (1994). Comparison of raindrop size distribution measurements by a Joss-Waldvogel disdrometer, a PMS 2DG spectrometer, and a POSS Doppler radar. *Journal of Atmospheric and Oceanic Technology*, *11*(4), 874–887. https://doi.org/10.1175/1520-0426(1994)011<0874:corsdm>2.0.co;2

Skofronick-Jackson, G., Petersen, W. A., Berg, W., Kidd, C., Stocker, E. F., Kirschbaum, D. B., et al. (2017). The global precipitation measurement (GPM) mission for science and society. *Bulletin of the American Meteorological Society*, *98*(8), 1679–1695. https://doi.org/10.1175/BAMS-D-15-00306.1

Smith, P. L. (2003). Raindrop size distributions: Exponential or gamma—Does the difference matter? *Journal of Applied Meteorology*, *42*(7), 1031–1034. https://doi.org/10.1175/1520-0450(2003)042<1031:rsdeog>2.0.co;2

Speirs, P., Gabella, M., & Berne, A. (2017). A Comparison between the GPM dual-frequency precipitation radar and ground-based radar precipitation rate estimates in the Swiss Alps and Plateau. *Journal of Hydrometeorology*, *18*(5), 1247–1269. https://doi.org/10.1175/JHM-D-16-0085.1

Straka, J. M., Zrnić, D. S., & Ryzhkov, A. (2000). Bulk hydrometeor classification and quantification using polarimetric radar data: Synthesis of relations. *Journal of Applied Meteorology*, *39*(8), 1341–1372. https://doi.org/10.1175/1520-0450(2000)039<1341:bhcaqu>2.0.co;2

Tokay, A., Bashor, P. G., Habib, E., & Kasparis, T. (2008). Raindrop size distribution measurements in tropical cyclones. *Monthly Weather Review*, *136*(5), 1669–1685. https://doi.org/10.1175/2007MWR2122.1

Tokay, A., Petersen, W. A., Gatlin, P., & Wingo, M. (2013). Comparison of raindrop size distribution measurements by collocated disdrometers. *Journal of Atmospheric and Oceanic Technology*, *30*(8), 1672–1690. https://doi.org/10.1175/JTECH-D-12-00163.1

Tokay, A., & Short, D. A. (1996). Evidence from tropical raindrop spectra of the origin of rain from stratiform versus convective clouds. *Journal of Applied Meteorology and Climatology*, *35*(3), 355–371. https://doi.org/10.1175/1520-0450(1996)035<0355:eftrso>2.0.co;2

Ulbrich, C. W., & Lee, L. G. (2002). Rainfall characteristics associated with the remnants of tropical storm helene in upstate South Carolina. *Weather and Forecasting*, *17*(6), 1257–1267. https://doi.org/10.1175/1520-0434(2002)017<1257:rcawtr>2.0.co;2

Vitale, J., & Ryan, T. (2013). Operational recognition of high precipitation efficiency and low-echo-centroid convection. *Journal of Operational Meteorology*, *1*(12), 128–143. https://doi.org/10.15191/nwajom.2013.0112

Vivekanandan, J., Adams, W. M., & Bringi, V. N. (1991). Rigorous approach to polarimetric radar modeling of hydrometeor orientation distributions. *Journal of Applied Meteorology and Climatology*, *30*(8), 1053–1063. https://doi.org/10.1175/1520-0450(1991)030<1053:ratprm>2.0.co;2

Wang, Y., & Chandrasekar, V. (2009). Algorithm for estimation of the specific differential phase. *Journal of Atmospheric and Oceanic Technology*, *26*(12), 2565–2578. https://doi.org/10.1175/2009JTECHA1358.1

Warren, R. A., Protat, A., Siems, S. T., Ramsay, H. A., Louf, V., Manton, M. J., & Kane, T. A. (2018). Calibrating ground-based radars against TRMM and GPM. *Journal of Atmospheric and Oceanic Technology*, *35*(2), 323–346. https://doi.org/10.1175/jtech-d-17-0128.1

Weatherford, C. L., & Gray, W. M. (1988). Typhoon structure as revealed by aircraft reconnaissance. Part I: Data analysis and climatology. *Monthly Weather Review*, *116*(5), 1032–1043. https://doi.org/10.1175/1520-0493(1988)116<1032:tsarba>2.0.co;2

Wilson, J. W., & Pollock, D. M. (1974). Rainfall measurements during hurricane Agnes by three overlapping radars. *Journal of Applied Meteorology and Climatology*, *13*(8), 835–844. https://doi.org/10.1175/1520-0450(1974)013<0835:rmdhab>2.0.co;2

Wu, Z., Zhang, Y., Zhang, L., Hao, X., Lei, H., & Zheng, H. (2019). Validation of GPM precipitation products by comparison with ground-based parsivel disdrometers over Jianghuai region. *Water*, *11*(6), 1260. https://doi.org/10.3390/w11061260

You, C., Kang, M., & Lee, D.-I. (2019). Rainfall estimates with respect to rainfall types using SSS-band polarimetric radar in Korea. *Atmosphere*, *10*(12), 773. https://doi.org/10.3390/atmos10120773

Zhang, P., Zrnić, D., & Ryzhkov, A. (2013). Partial beam blockage correction using polarimetric radar measurements. *Journal of Atmospheric and Oceanic Technology*, *30*(5), 861–872. https://doi.org/10.1175/JTECH-D-12-00075.1

Zheng, H., Zhang, Y., Zhang, L., Lei, H., & Wu, Z. (2021). Precipitation microphysical processes in the inner rainband of tropical cyclone Kajiki (2019) over the South China sea revealed by polarimetric radar. *Advances in Atmospheric Sciences*, *38*(1), 65–80. https://doi.org/10.1007/s00376-020-0179-3

Zrnic, D. S., & Ryzhkov, A. (1999). Polarimetry for weather surveillance radars. *Bulletin of the American Meteorological Society*, *80*(3), 389–406. https://doi.org/10.1175/1520-0477(1999)080<0389:PFWSR>2.0.CO;2